The Mastcam-Z Radiometric Calibration Targets on NASA's Perseverance Rover: Derived Irradiance Time-Series, Dust Deposition, and Performance over the First 350 Sols on Mars.

M. Merusi[1], K.B. Kinch[1], M.B. Madsen[1], J.F. Bell III[2], J.N. Maki[3], A.G. Hayes[4], J. Joseph[4], J.R. Johnson[5], M. Rice[6], E.A. Cloutis[7], D. Applin[7], M.T. Lemmon[8], A.F. Vaughan[9], J.I. Núñez[5], E. Jensen[10], J.Z. Kristensen[1], K. Paris[2], E. Cisneros[2], M.R. Kennedy[10], O. Gasnault[11].

[1]Niels Bohr Institute, University of Copenhagen, Copenhagen, Denmark

[2]School of Earth and Space Exploration, Arizona State University, Tempe, AZ, USA

[3]Jet Propulsion Laboratory, California Institute of Technology, Pasadena, CA, USA.

[4]Department of Astronomy, Cornell University, Ithaca, NY, USA

[5]Johns Hopkins University Applied Physics Laboratory, Laurel, MD, USA

[6]Geology Department, Western Washington University, Bellingham, WA, USA

[7]Department of Geography, University of Winnipeg, Winnipeg, Manitoba, Canada

[8]Space Science Institute, Boulder, CO, USA

[9]USGS Astrogeology Science Center, Flagstaff, AZ

[10]Malin Space Science Systems, San Diego, CA, USA

[11]Institut de Recherche en Astrophysique et Planétologie (IRAP), Université de Toulouse, CNRS, CNES, Toulouse – France

Corresponding author: Marco Merusi (`marco.merusi@nbi.ku.dk`)

Key Points

- The Mastcam-Z Calibration Targets ensured quality and stability in the reflectance calibration of images over the first 350 sols on Mars.
- Dust deposited frequently on the deck of the rover and on the calibration target surfaces, especially on its permanent magnets.
- A small offset in the fits used for calibration and a yellowing effect of one material were observed and will be further investigated.

Abstract

The Mastcam-Z radiometric calibration targets mounted on the NASA Perseverance rover proved to be effective in the calibration of Mastcam-Z images to reflectance (I/F) over the first 350 sols on Mars. Mastcam-Z imaged the calibration targets regularly to perform reflectance calibration on multispectral image sets of targets on the Martian surface. For each calibration target image, mean

radiance values were extracted for 41 distinct regions of the targets, including patches of color and grayscale materials. Eight strong permanent magnets, placed under the primary target, attracted magnetic dust and repelled it from central surfaces, allowing the extraction of radiance values from eight regions relatively clean from dust. These radiances were combined with reflectances obtained from laboratory measurements, a one-term linear fit model was applied, and the slopes of the fits were retrieved as estimates of the solar irradiance and used to convert Mastcam-Z images from radiance to reflectance. Derived irradiance time series are smoothly varying in line with expectations based on the changing Mars-Sun distance, being only perturbed by a few significant dust events. The deposition of dust on the calibration targets was largely concentrated on the magnets, ensuring a minimal influence of dust on the calibration process. The fraction of sunlight directly hitting the calibration targets was negatively correlated with the atmospheric optical depth, as expected. Further investigation will aim at explaining the origin of a small offset observed in the fit model employed for calibration, and the causes of a yellowing effect affecting one of the calibration targets materials.

Plain Language Summary

The calibration targets of Mastcam-Z camera, mounted on the NASA Perseverance rover, are used to calibrate Mastcam-Z images from units of radiance to reflectance. Reflectance expresses how the sunlight is reflected by geologic targets under different geometries and wavelengths to give insights on their nature. The radiances measured within calibration targets were combined with known reflectances to obtain estimates of the local sunlight. These estimates were used to calibrate Mastcam-Z images. Our analysis shows that the calibration targets ensured a high quality of calibration over the first 350 sols (martian days) on Mars. The sunlight derived from the measurements can be monitored in time and shows a smooth trend with variations due to the changing distance between Mars and the Sun, and larger disturbances due to significant amounts of dust raised in the atmosphere by the wind. This dust settled on the top surface of the rover, but it minimally affected the calibration process. We also noticed that when the atmosphere is rich in dust, less sunlight can make it to the surface, and vice-versa. More investigation will aim at explaining small variations in our calibration model and a weird effect affecting one of the materials of the calibration targets.

1. Introduction

NASA's Mars 2020 Perseverance Rover mission (Farley *et al.*, 2020) was launched from Cape Canaveral (FL) on July 30$^{\text{th}}$, 2020 and landed successfully within Jezero crater on February 18$^{\text{th}}$, 2021. During its first 350 sols on Mars, Perseverance achieved a number of significant milestones in planetary exploration, including the completion of a campaign of scientific investigation of the floor of Jezero crater (Mangold *et al.*, 2021), the successful helicopter Ingenuity technology demonstration (Balaram *et al.*, 2021), the extraction of six rock core samples, and driving almost 4 km. Among its seven scientific

instruments, the Mastcam-Z cameras (Bell *et al.*, 2021) captured thousands of images. Mastcam-Z is a multispectral, stereoscopic pair of cameras capable of multiple focal lengths mounted on the rover's mast. It consists of two CCD sensors with Bayer pattern that can acquire broad-band Red/Green/Blue color images when imaging through a broad IR-cutoff filter. In addition, 12 narrow-band filters (six for each sensor, or 'eye') span visible and near-infrared wavelengths from 440 to 1022 nm. In order to correctly calibrate Mastcam-Z images to units of reflectance, the camera relies on a set of calibration targets (Kinch *et al.*, 2020), or cal-targets, fixed on the deck of the rover. During the first 350 sols on Mars, the cal-targets were the most imaged objects by Mastcam-Z.

In this manuscript we show the methods that were employed to extract radiometric data from the images of the cal-targets and the main results, including their performance based on calibration models, the time evolution of the derived solar irradiance, a basic assessment of the deposition of dust on the cal-targets surfaces and its nature, the observed fraction of direct sunlight versus diffuse illumination, and its dependence on the optical depth of the martian atmosphere. We also discuss an observed offset in the linear relation between radiance and reflectance, and a "yellowing effect" on the white patch of the cal-targets.

In section 2 we present the cal-targets and the basic concept of the reflectance calibration. Section 3 is a summary of the methods used to obtain our results, including the selection of regions of interest of the cal-targets, the computation of the solar irradiance through linear fits and the storage of the cal-targets radiometric data. In section 4 we report all the results concerning the calibration and performance of the cal-targets in the first 350 sols, the dust deposition on the cal-targets and its spectral characteristics, and the relation between direct and diffuse solar light in time with a reference to the atmospheric optical depth. Furthermore, we discuss the observed offset in the linear radiance-reflectance relation. In section 5 we evaluate the general performance of the cal-targets and the overall performance of the current calibration procedure, based on variations in the dust and the environment.

1. The Mastcam-Z Radiometric Calibration Targets

The Mastcam-Z Calibration Targets (Kinch *et al.*, 2020), or cal-targets, are a pair of physical devices mounted on the Perseverance rover deck (Figure 1) and primarily used to assist in the conversion of Mastcam-Z images from units of radiance to reflectance (I/F). They were designed and assembled at the Niels Bohr Institute of the University of Copenhagen.

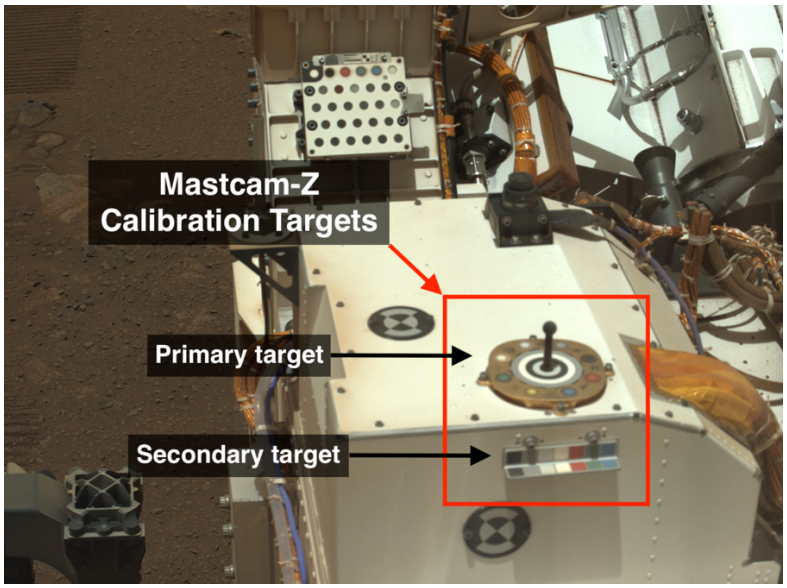

Figure 1. Context image of the Mastcam-Z primary and secondary calibration targets, taken by the left eye of Mastcam-Z (L0) on sol 23 at 26 mm focal length (Image-ID: ZLF_0023_0668982043_596FDR_N0030770ZCAM03003_0260LMJ, sequence ZCAM03003). In the upper center, the SuperCam calibration target is also visible.

The principal device, known as "primary target", is bolted to the top of the Rover Pyro Firing Assembly (RPFA) and consists of eight round color and grayscale ceramic patches, four concentric grayscale rings and a central shadow post fixed on a gold-plated aluminum frame. The circular patches, mounted in the periphery of the primary target, are four in colors (here referred to as blue, green, yellow, red) and four in grayscales (black, dark gray, light gray, white). Eight hollow-cylindrical magnets are mounted underneath the round patches. These Sm_2Co_{12} magnets are strongly magnetized along the axis of symmetry. They attract even weakly magnetic (in the sense of having significant magnetic susceptibility) martian dust grains on the external annular portion of the patches, while actively repelling such grains from the central circular part, leaving it relatively clean from dust. The grayscale rings placed in the center of the target are the same colors and materials as the peripheral grayscale patches. From the innermost to the outermost, the colors of the rings are light gray, black, white, and dark gray. The shadow post (or gnomon) is placed at the center of the rings and painted with an IR-black paint. The base of the primary target is made from aluminum with silver and gold anodization and fits inside a square with a side of 98 mm. The "secondary target" is fixed on the vertical side of the RPFA just below the primary target, in direct sight of Mastcam-Z, and contains two rows of seven square tiles each mounted on an aluminum frame. One row is situated parallel to the plane of the rover deck, while the other row is situated

perpendicularly. Both rows have the same color tiles, with the colors being the same as the round patches of the primary target except for the yellow. From left to right, as seen from Mastcam-Z, they are black, dark gray, light gray, white, red, green, and blue. The horizontal length of the secondary target is 80 mm. For a complete technical description of the calibration targets and their heritage from previous Mars rovers, see Kinch *et al.* (2020).

In this work we adopt a simple nomenclature scheme for the different patches and rings according to their positions, which is illustrated in Figure 2. In the primary target, the inner circular portions of the eight round patches are named "central spots" or "clean spots", while the external annular portions, which lie over the magnets, are called "magnet rings", not to be confused with the four concentric grayscale rings at the center of the primary target. The name "clean spots" is a consequence of the action of the magnet rings, which capture the magnetic fraction of the airborne dust. For the secondary target, the square patches are named "secondary horizontal tiles" or "secondary vertical tiles", depending on their orientation.

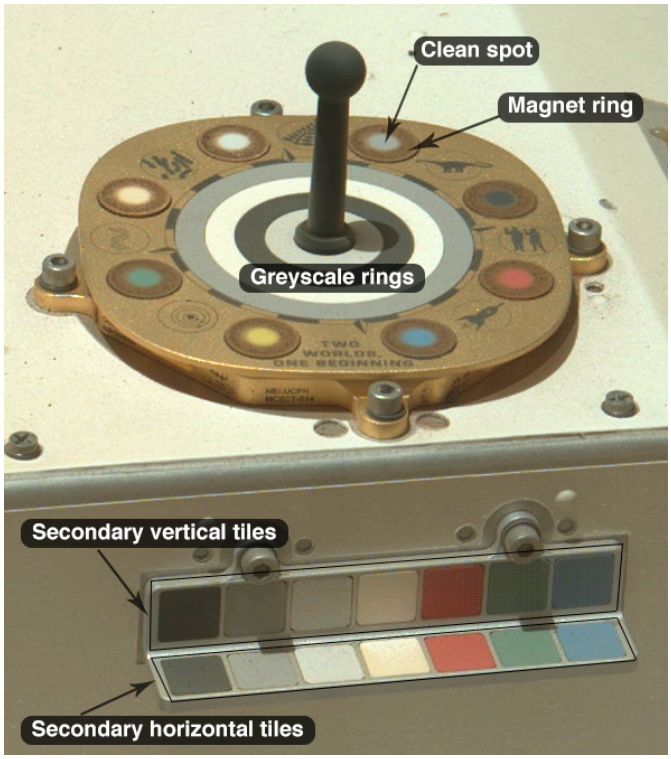

Figure 2. The Mastcam-Z Calibration Targets imaged by the left eye (L0) of Mastcam-Z on sol 180 at 48 mm zoom (Image ID: ZL0_0180_0682919878_394ECM_N0062666ZCAM03014_04
sequence ZCAM03014). The main regions of the primary and secondary targets are indicated with the names used in this work.

From landing to sol 350, Mastcam-Z acquired 2578 images of the cal-targets. Among those images, and all the filters of Mastcam-Z, the L0/R0 Red/Green/Blue (RGB) Bayer broadband filters installed within the sensors of the two eyes of the camera were the most used, not only for calibration as part of multispectral sequences but also to obtain color images for testing and verification of the camera and the calibration targets, photometric analysis, and public outreach. The distribution of images taken among the filters of Mastcam-Z is listed in table 1. The RGB images in the two eyes are considered as "single shot" images, but they can be split into three frames corresponding to their three Bayer components (named L0R, L0G, L0B for the left eye and R0R, R0G, R0B for the right eye), each one covering a different spectral range. Of the 2578 images mentioned above, 344 were transmitted lossless, without any lossy compression. The remaining 2234 were transmitted using an 85% quality level compression.

Filter name	Range [nm]	Total images	Filter name	Range [nm]	Total images
L0B	480 ± 46	197	R0B	480 ± 46	197
L0G	544 ± 41		R0G	544 ± 42	
L0R	630 ± 43		R0R	631 ± 43	
L1	800 ± 9	185	R1	800 ± 9	185
L2	754 ± 10	179	R2	866 ± 10	185
L3	677 ± 11	179	R3	910 ± 12	179
L4	605 ± 9	179	R4	939 ± 12	179
L5	528 ± 11	185	R5	978 ± 10	179
L6	442 ± 12	185	R6	1022 ± 19	185

Table 1. Summary of the total number of images of the Calibration Targets taken by Mastcam-Z in each filter within the first 350 sols on Mars. For each filter, the corresponding spectral range is reported.

These images were captured by Mastcam-Z at several illumination geometries relative to the cal-targets. The illumination geometry of an observation is described by three angles. We define these three angles as *incidence*, *emission* and *azimuth*. The incidence angle ($0^\circ \leq i \leq 90^\circ$) is measured between the zenith of the target and the Sun-target direction, the emission angle ($0^\circ \leq e \leq 90^\circ$) is measured between the zenith of the target and the detector-target direction, while the azimuth angle ($0^\circ \leq \mathrm{Az} \leq 180^\circ$ for hemispheric symmetry) is measured on the plane of the target and is the angle between the planes of incidence and emission. The angles i and e are measured from the zenith. The emission angle is fixed by the geometry of the rover with the primary and secondary targets seen by Mastcam-Z under emission angles of approximately 58° and 54°, respectively. The overall distributions of the incidence and azimuth angles of the cal-targets images are reported in Figure 3. Given the changing orientations of Perseverance, the azimuth angles are evenly distributed, though with a larger frequency in the 5°-10° interval, which corresponds to the Sun being approxi-

mately behind Mastcam-Z during the observation (Sun in front of the rover), and a much lower frequency of observations at opposite azimuth. In addition, most observations were made with the Sun relatively high above the horizon, with 88% of images taken at incidence angles lower than 30° and a peak around 10°-15° (see Figure 3).

As studied by Buz *et al.* (2019) and by Kinch *et al.* (2020) in the pre-flight tests, at the typical emission angle of 58° all the color and grayscale materials of the cal-targets (though to a lesser extent for the white patches) show a strong forward scattering peak with incidence angles $> 45°$. The smaller number of observations on Mars with the Sun opposite to the camera (high azimuth) reduced the impact of the forward scattering, which in some cases ($i \geq 50°$) was quite significant. In addition, at higher incidence angles the diffuse light acquired importance within the dusty atmosphere, reducing the contrast between the sunlit and shadowed regions. Early martian morning or late afternoon observations proved challenging for estimating the solar irradiance as part of the reflectance calibration, and this will serve as a starting point for improvements in our data processing in the future. The best estimates of the irradiance were obtained when the Sun was high in the sky, with a smaller atmospheric path length and negligible forward or backward scattering. Mastcam-Z acquired most cal-target images at incidence angles lower than 30°. However, since the diffuse light had a major impact at low Sun, this geometry was particularly useful to monitor the dust suspended in the atmosphere. This was done by comparing the radiance from the regions in the gnomon shadow on the grayscale rings to those in the direct sunlight (see sect. 4.4.2).

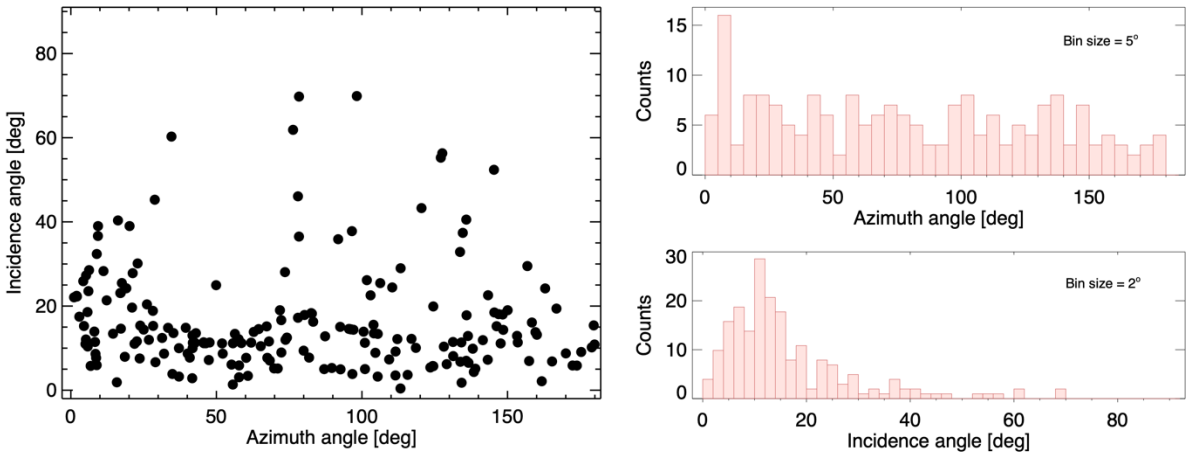

Figure 3. Distributions of incidence and azimuth angles of all the 197 cal-targets image sequences. Each dot in the incidence-vs-azimuth plot on the left, corresponding to an entry in the histograms on the right, is a single cal-targets sequence, which includes at least one image for each eye of Mastcam-Z in the same observation (in most cases it is in all filters or only in L0/R0).

1. The Radiance-to-Reflectance Calibration

The primary objective of the cal-targets is the generation of reflectance-calibrated images. As a last step of the radiometric calibration, all Mastcam-Z images in units of radiance (i.e., $W/(m^2 \bullet \text{ nm} \bullet \text{sr})$), (Hayes *et al.*, 2021), are calibrated to radiance factor I/F (or IOF), where I is the radiance from the scene and F is the instantaneous solar irradiance. IOF is defined as the reflectance relative to that of a perfect Lambertian scatterer illuminated from the zenith. While the radiance can be measured, the local irradiance F is challenging to model at the martian surface due to its dependency on illumination geometries and atmospheric conditions that change over short timescales. To address this directly, frequent imaging of the cal-targets in all filters is performed (in general cal-target images accompanied any multispectral observation of surface targets).

The following equation is used to convert radiance images into IOF (Kinch et al, 2020):

$$\text{Image}_{\text{IOF}} = \text{CT}_{\text{IOF}} \frac{\text{Image}_{\text{RAD}}}{\text{CT}_{\text{RAD}}} \ , \quad (1)$$

where $\text{Image}_{\text{RAD}}$ and CT_{RAD} are the pixel-by-pixel measured radiances of the image to calibrate and the cal-targets, respectively, and CT_{IOF} is the reflectance of the cal-targets, which is known from laboratory spectra. The IOF calibration allows the extraction of reflectance spectra of interesting terrain units and specific geologic targets that can be consistently compared and for which the nature can be assessed in detail (e.g., from this issue: Garczynski *et al.*, Horgan *et al.*, Núñez *et al.*, Rice *et al.*, Vaughan *et al.* for Mastcam-Z reflectance data, and Royer *et al.*, Mandon *et al.*, for SuperCam data). In addition, frequent estimates of the solar irradiance F constrain atmospheric conditions and dust displacement over time.

IOF values can be converted to units of reflectance factor R* through the equation:

$$R^* = \frac{\text{IOF}}{cos(i)} \ , \quad (2)$$

where i is the incidence angle of the observation. This, of course, requires knowledge of i or alternatively a simplifying assumption (e.g., modeling the martian surface as a flat plane). R* is defined as the reflectance relative to that of a perfect Lambertian scatterer illuminated in the same geometry as the observation.

1. **Methods**

   (a) **Selection of the Regions of Interest on the Calibration Tar-**

gets

In the practical implementation of the IOF calibration, the radiance values of the eight primary clean spots (expected to be the least dusty surfaces) were extracted. The process of selection of these regions was part of a more general context, which aimed at collecting the average radiance values of all the main areas, named Regions of Interest (ROIs), of the cal-targets. This process was similar to that implemented for MER (Bell *et al.*, 2003, 2007) and MSL (Bell *et al.*, 2017) calibration targets. The selection of ROIs was made automatically by an algorithm that overlaid two model templates of the cal-targets (one for each eye) on the cal-target images, in which each region within the template was represented by a different color (Figure 4). This operation required regular human intervention, usually in order to manually edit the regions when the algorithm did not recognize shadows.

Figure 4. Example of ROI selections over an image of the cal-targets taken by the left eye of Mastcam-Z in the L1 filter (800 nm) on sol 69 at 48 mm focal length (Image-ID: ZL1_0069_0673052731_973ECM_N0032208ZCAM03014_048085J01, seq. ZCAM03014). All 41 regions of interest are visible in colors, including those under the gnomon's shadow on the grayscale rings. The two ROI's

partially selected in the secondary target were edited to exclude the shadows due to the bolts of the support.

The maximum number of ROIs was 41, though not all of them were always selectable due to the position of the gnomon shadow on the grayscale rings, which depended on the incidence and azimuth angles. For these reasons, the number of ROIs on the grayscale rings within the gnomon shadow ranged from 0 to 4. On sols 3, 206, 290 and 305 some clean spots appeared shadowed by the gnomon owing to low Sun angles. More commonly, shadowing of one or both rows of the secondary target occurred due to its location on the side of the RPFA.

Once all the ROIs were selected suitably, their locations were documented along with the average and standard deviation of measured radiances over their pixels. The list of ROI groups is reported in table 2.

Target	Regions	Number of selections
Primary	Clean spots	8
Primary	Magnet rings	8
Primary	Sunlit grayscale rings	4
Primary	Grayscale rings in the gnomon shadow	Up to 4, depending on gnomon shadow size and observa
Secondary	Horizontal tiles	7
Secondary	Vertical tiles	7
All scene	Primary target and deck	3 (portion of deck, portion of the golden base and top c

Table 2. Summary of the main groups of Regions of Interests of the cal-targets. For each group, the target, the position on the target and the number of selections are listed.

1. **The Extraction of Solar Irradiance through Linear Fits**

The solar irradiance is F. F was computed as the CT_{RAD}/CT_{IOF} ratio of equation (1). Since there are eight clean spots, there are eight possible versions of this equation. In practice, therefore, this consisted of examining one-term linear fits between the eight measured radiances and the eight model reflectances, with F extracted as the slope of the fit.

The measured radiances were computed as the averages over the pixels of the clean spot ROIs. The model reflectances were obtained through visible/near-infrared (400-2500 nm) laboratory measurements of the same eight color and grayscale samples at different geometries across the visible and near infrared spectrum (Kinch *et al.*, 2020; Buz *et al.*, 2019).

For every image of the cal-targets in any filter one single radiance-vs-reflectance fit was made. The left plot of Figure 5 shows an example of such fit on the radiances and reflectances of the eight primary clean spots extracted from a cal-targets image in filter L1 (800 nm) that was taken by Mastcam-Z before launch

at NASA ATLO (Assembly, Test and Launch Operations) facility, with the cal-targets illuminated at incidence angle $i = 0^{\circ}$ by artificial light. After deriving F from the slope of the fit, this value was then applied through equation (1) to the pixels of all the Mastcam-Z radiance-calibrated images in the same filter, yielding reflectance spectra such as the cal-target spectra shown in Figure 5 on the right.

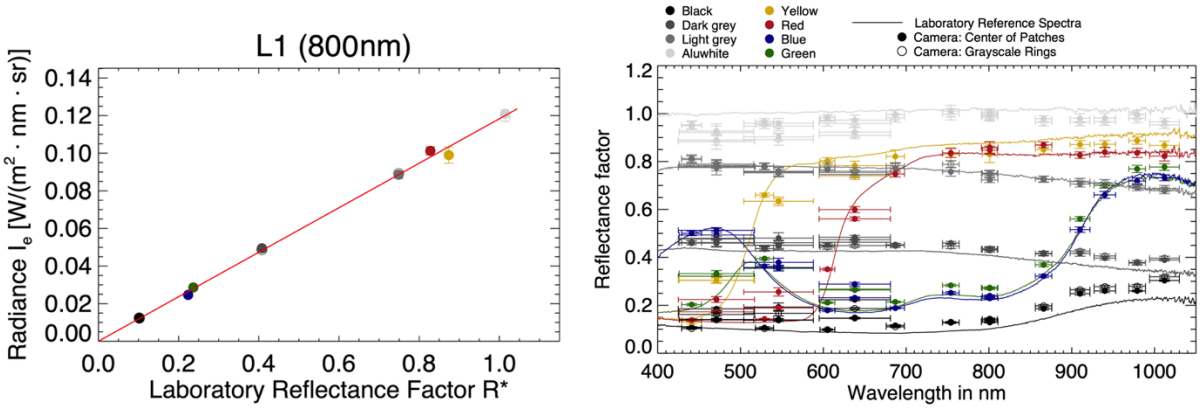

Figure 5. On the left: example of one-term linear fit extracted from a Mastcam-Z image of the cal-targets in filter L1 (800 nm) during the pre-flight tests on the Perseverance rover at NASA ATLO (Assembly, Test and Launch Operations) facility. The red line is the fit. On the right: cal-targets spectra at ATLO. The solid lines are the laboratory reference spectra. In both plots, the filled circles are the primary clean spots, while the open circles represent the grayscale rings. The cal-targets were illuminated by artificial light with $i = 0^{\circ}$.

1. **The Radiometric Coefficients Files**

A major portion of the cal-targets sequence processing included the generation and storage of information on the images and their ROI selections. We refer to these as Radiometric Coefficients files, or simply RC-files, which were created simultaneously with the linear fits described in section 3.2. The first part of a typical RC-file included metadata (e.g., name of the corresponding cal-target image, local martian time of the original image). The body of the file included a list of arrays, each of which was formed by 41 fields (one for each ROI selection). The algorithm that selected the ROIs for each region included the complete name of the region, its average radiance over the pixels and uncertainty of this radiance, number of pixels selected, illumination geometry angles and model reflectance related to the color material and to the geometry of the region. The inverse of the slope of the linear fit described in section 3.2 was also included in the RC-files, along with three Boolean arrays of flags (expressed in terms of 0 and 1) that specified which regions had been selected, which ones were "bad" and should not be used (usually due to unwanted shadows), and which should be used to make the linear fits for calibration. We used a graphic interface to

mark the regions appropriately. Whenever a region had not been selected, its place in the data arrays of the RC-files did not show any numerical value. An example of an RC-file is given in appendix 1.

1. **Results**

All quantitative results that we present here have been obtained from the values stored in the entire set of RC-files covering the time range from landing to sol 350. In each color image in L0 and R0, one RC-file was extracted individually from each of the three broad-band channels (L0B, L0G, L0R, and R0B, R0G, R0R). Hence, the total number of RC-files in our set was 3366. The regions of the cal-targets that were not selected or were marked as bad were not included in the following analysis.

1. **Imaging of the Calibration Targets on Mars**

The considerable number of color images of the cal-targets acquired by Mastcam-Z allowed a regular visual check of its conditions over time, including the accumulation and displacement of airfall dust and monitoring the color and grayscale materials.

Figure 6 is a comparison of four example Bayer RGB images of the cal-targets taken by the left eye of Mastcam-Z. The most evident details that can be visually evaluated in time are the progressive change of hue of the primary white patch and the accumulation of dust and sand on the surfaces. The former is a "yellowing" effect that degraded the visible layer of the white material (AluWhite98) since landing. A more detailed treatment of the problem is reported in section 4.6.

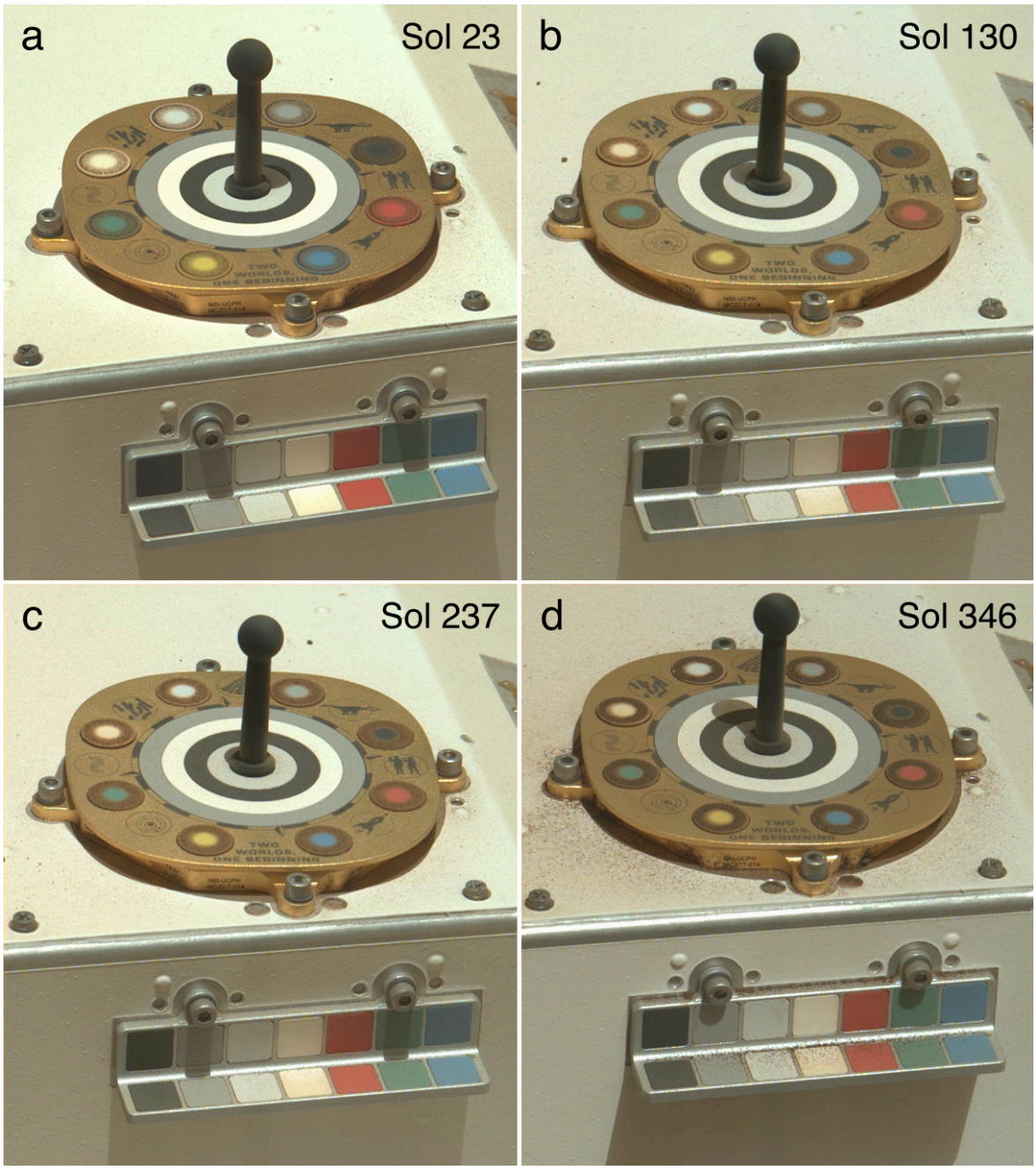

Figure 6. Appearance of the calibration targets in 4 Mastcam-Z color images taken by the left eye on (a) sol 23, (b) sol 130, (c) sol 237 and (d) sol 346. Image (a) was acquired at 63 mm zoom and had sequence number ZCAM03003, while

(b), (c) and (d) at 48 mm and had sequence number ZCAM03014. Image-IDs: (a) ZLF_0023_0668982767_596FDR_N0030770ZCAM03003_0630LMJ01, (b) ZL0_0130_0678477333_428ECM_N0042222ZCAM03014_048085J01, (c) ZL0_0237_0687977979_443ECM_N0072050ZCAM03014_048085J01, (d) ZL0_0346_0697653263_269ECM_N0092982ZCAM03014_048085J01.

Figure 6 also illustrates the progressive increase in magnetic dust with time on the primary magnet rings, manifested as an overall dark reddish color. This outcome, which was also observed on the MER (Madsen *et al.*, 2009) and MSL (Bell *et al.*, 2017) rovers, was expected from the cal-targets design. The underlying colors, that were already attenuated but still visible after the first sols (Fig. 6a), were not as discernible at the end of the period under analysis in this work (Fig. 6d). On other surfaces, such as the other parts of the cal-targets or the deck surroundings, the deposition seemed to be ruled by either original deposition of small grains during the landing event, wind activity capable of transporting larger grains on top of the deck, and/or airfall dust. In general, airfall dust and larger grains were displaced frequently, allowing the cal-targets to remain rather clean. In addition, the deposition of dust on the secondary target was affected by its position on a vertical surface, which would limit the fraction of dust falling on the horizontal tiles. During the first 350 sols of the mission Perseverance experienced several significant episodes of high wind and local dust lifting. The strongest event occurred between sols 314 and 316 (Lemmon *et al.*, 2022), with consequences visible for several sols (Fig. 6d). Appreciable layers of brownish airfall dust and sand were conspicuous on the grayscale rings, on the deck next to the primary target (including the vertical side of the golden base), and on the secondary horizontal target following this event.

Since the ROIs that were normally used for IOF calibration were the eight clean spots, it is interesting to show some statistics of the number of pixels for the corresponding eight regions at three zoom settings: the two extremes (26 mm and 110 mm) and the most employed zoom setting (48 mm). The 26 mm zoom was used to image the cal-targets only at the beginning of the mission, between sols 9 and 26, in a total of 54 frames. The average number of pixels over the eight regions and the 54 frames was approximately 15. For the 110 mm zoom, the average on the values obtained on Mars (42 frames) was 396 pixels. Kinch *et al.* (2020) considered the shapes of the clean spots as ellipses when seen from Mastcam-Z, retrieving their major and minor axes respectively of 10 by 5 pixels for the 26 mm zoom and 40 by 20 pixels for the 110 mm zoom. These numbers give areas of 40 and 630 pixels, respectively. The values that we obtained were lower than these estimates, likely because their prediction was computed over the entire surface of the clean spots. The algorithm that selected those regions always picked a smaller central portion of the clean spots, leaving a reasonable margin from the boundary of the magnet rings in order not to select dusty pixels that could systematically affect our measurements. However, 93% of the total number of cal-target images in the first 350 sols of the mission were captured with a 48 mm focal length. For this setting, the average number of pixels was 67.

1. **Cross-Instrument Observations of the Mastcam-Z Calibration Targets**

Due to its exposed location on the deck of the rover, the Mastcam-Z cal-targets could also be imaged by other cameras of the rover, in particular the EDL (Entry, Descent and Landing) camera, WATSON and SuperCam Remote Micro-Imager (RMI).

One of the first images of the rover (and the cal-targets in particular) within the martian environment is shown in Figure 7 and was taken on February 18$^{\text{th}}$, 2021, at 20:55 UTC by the Down-Look EDL Camera (Maki *et al.*, 2020) mounted on the descent stage (also known as the "skycrane"). It shows the Perseverance rover being taken down to a few meters from the martian surface by the rocket powered skycrane, which subsequently placed gently the six wheels of the rover on the surface, then disconnected by cutting the three cables and flew away.

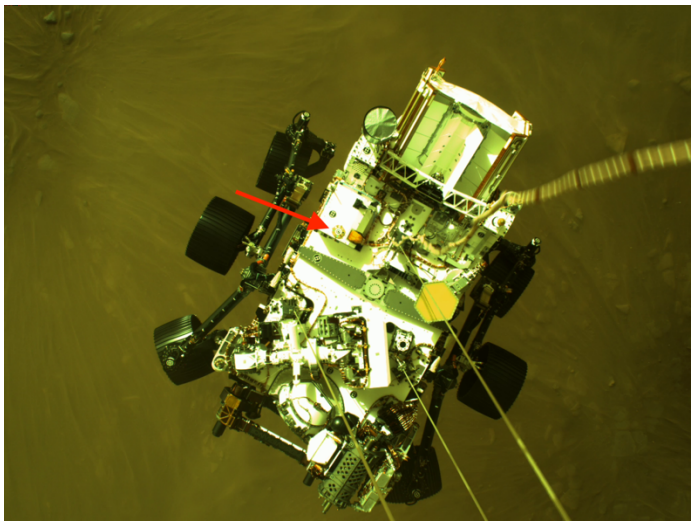

Figure 7. One of the video-frames from the down-look camera mounted on the sky crane showing the Perseverance rover being lowered onto the martian surface through cables on February 18$^{\text{th}}$, 2021 (Image-ID: ESF_0001_0667022251_842ECV_N0010052EDLC00001_0010LUJ01, seq. EDLC00001). The red arrow indicates the location of the Mastcam-Z calibration targets.

The WATSON camera of the SHERLOC instrument (Bhartia *et al.*, 2021) mounted at the end of the robotic arm of the rover captured images of the pristine Mastcam-Z cal-targets on sol 26. The observation was intended for color calibration, since images of the cal-targets at the beginning of the mission, when the cal-targets were still relatively pristine, could be compared with future WATSON sequences. On sol 26, Mastcam-Z images of the cal-targets were paired with WATSON images very close in time by the SHERLOC team, in order to cross-calibrate between the two cameras. The WATSON images of

Mastcam-Z cal-targets of sol 26 are displayed in Figure 8a-b and were taken less than 1 hour after that from Mastcam-Z, which appears in Figure 8c. Of the two WATSON images of Figure 8, the former was acquired at 50 cm standoff, with the WATSON camera as close as physically possible to the cal-targets, whereas the latter was at 130 cm standoff, where the robotic arm was placed as close to the mast as possible to mimic the Mastcam-Z view of the cal-targets.

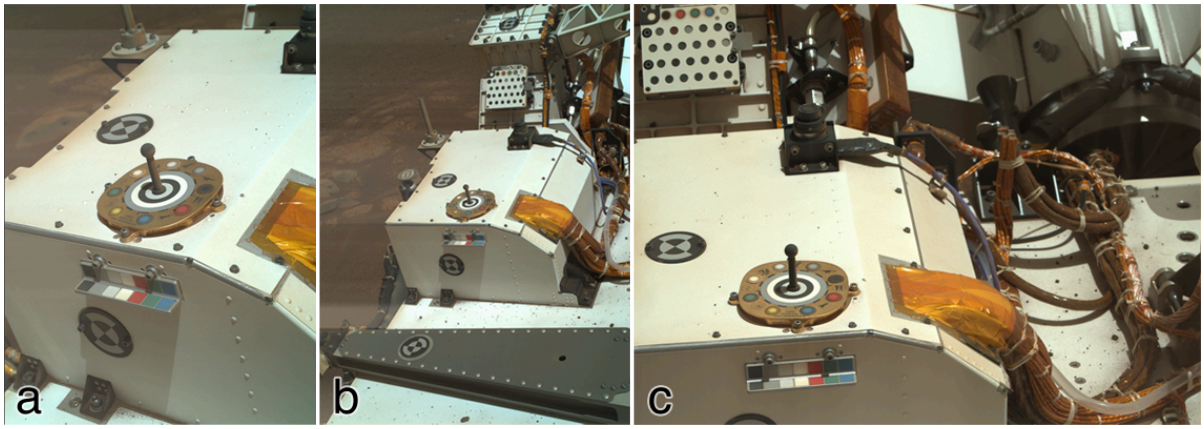

Figure 8. The Mastcam-Z cal-targets imaged on sol 26 by (a) the WATSON camera at 50 cm standoff (seq. SRLC07009) and (b) at 130 cm standoff (seq. SRLC07008), and (c) by the right eye of Mastcam-Z at 34 mm focal length (seq. ZCAM03004). The two WATSON images were captured approximately 40 minutes after the Mastcam-Z image. Image-IDs: (a) SIF_0026_0669252925_206EBY_N0030792SRLC07009_0000LUJ01, (b) SIF_0026_0669252754_132EBY_N0030792SRLC07008_0000LUJ02, (c) ZRF_0026_0669250585_064FDR_N0030792ZCAM03004_0340LMJ01.

Some of the patches of the primary and secondary target were imaged by the Remote Micro-Imager (RMI) of the SuperCam instrument (Maurice *et al.*, 2021) as part of ongoing calibration and monitoring activities. Figure 9 shows two examples of such high-resolution images, captured on sol 80 and 317, which portray the red and the white primary patches, respectively.

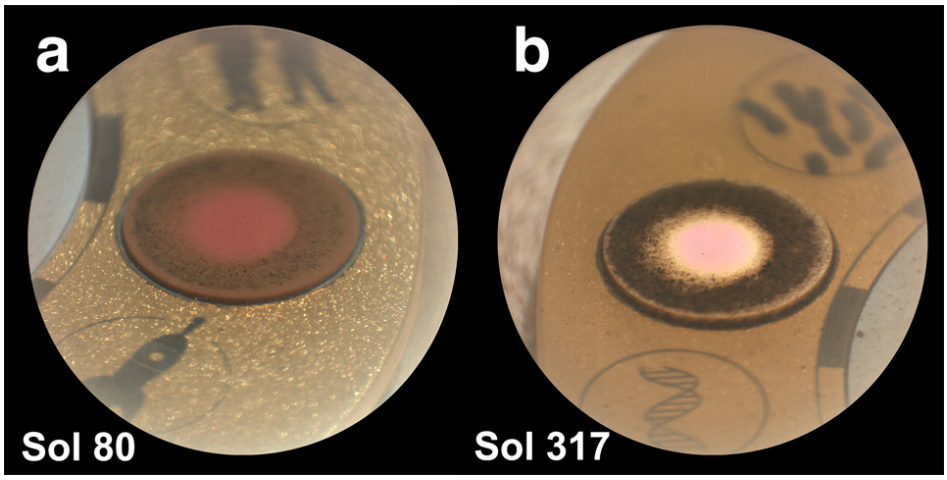

Figure 9. Two images of the Mastcam-Z cal-targets acquired by the Remote Micro Imager of SuperCam instrument: the red primary patch on sol 80 (seq. SCAM03080) and the white primary patch on sol 317 (seq. SCAM02317). Both images were contrast-stretched. Image-IDs: (a) LRF_0080_0674037938_567EBY_N0032430SCAM03080_0390I6J, (b) LRF_0317_0695080358_529EBY_N0090000SCAM02317_0370I6J.

1. **One-Term Fits and Calibration Target Spectra**

For every cal-target image calibrated to radiance, a unique RC-file documented the one-term linear fit between measured radiance and model reflectance factor R*. These fits were efficient indicators of the state of the clean spots in time and under different illumination geometries and atmospheric conditions. Figure 10 shows the fits relative to four different filters (L6, L3, R2 and R5) and three different sols of the mission (12, 178 and 346). One noticeable feature of the plots was the unexpected behavior of the white patch, whose change in visual appearance was already evident, as shown in Figure 6. Consequently, the white clean spot was never employed for the making of the fits. This is discussed in detail in section 4.6.

In general, the relative uncertainty on the slopes of the fits was included between 2.32% in R5 (978 nm) and 4.33% in L4 (605 nm), with a mean value of 3.34% over all filters. The datapoints consistently hint that the fitted line which is constrained to pass through the origin is not the very best line fit to the data, rather a line with a small positive constant term would be a better fit. This is unlike the similar tests carried out before launch (Fig. 5). We never employed an offset in our linear fit model for IOF calibration, but we investigated its time evolution (see section 4.5). As a reference, the one-term fits used for calibration had an average reduced chi-squared χ^2_{red} of 22.4, with values ranging from a minimum of 10.7 in R5 (978 nm) to a maximum of 34.4 in L2 (754 nm).

The spectral aspect of the primary clean spots obtained after the extraction of

the fit slope is shown in Figure 11 for sols 12 and 339 with their laboratory spectra. The radiometric decline of the white patch, more impactful at shorter wavelengths, is evident. All the other colors did not present any noticeable variation or deviation from the laboratory spectra, thus implying that those regions were not heavily affected by the deposition of airfall dust, likely due to the presence of the magnet rings. Also those regions were apparently not affected by the effect leading to the yellowing of the white material (AluWhite98).

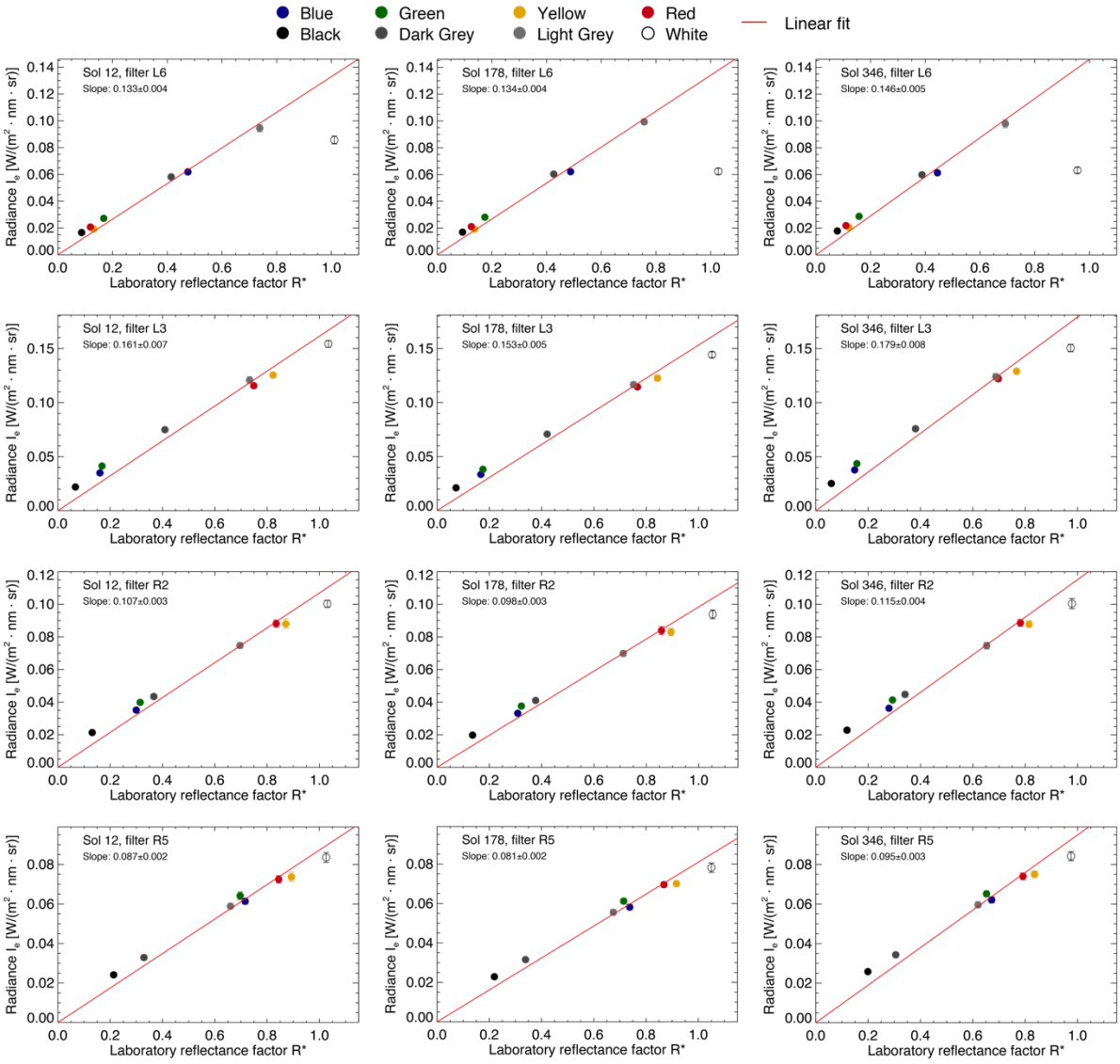

Figure 10. Examples of one-term linear fits over the datapoints of measured

radiance and model reflectance factor for three sols (sol 12, 178, 346, along the columns) in four filters (L6, L3, R2, R5, along the rows). The straight red lines are the fits. All the eight clean spots are plotted, but the white was not used to compute the fits.

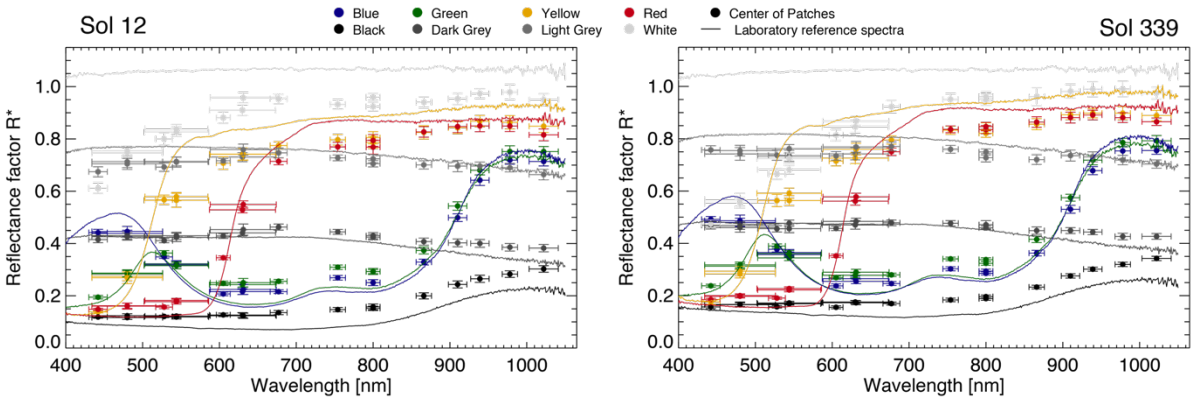

Figure 11. Calibration Target spectra from sol 12 and 339. The circles are the observed calibrated IOF reflectances of the clean spots, while the solid lines represent the corresponding laboratory spectra.

1. **Solar Irradiance Time Series**

The slopes of the one-term linear fits used for IOF calibration are indicators of the instantaneous solar irradiance. Because this could be affected by multiple factors, such as Sun-Mars distance, atmospheric conditions, dust and light diffusion, monitoring the slope values is an efficient way to evaluate indirectly the martian environment and its variations in time. In addition, the illumination geometry could influence the slope extracted from the fit, especially when the Sun is low on the horizon. Therefore, we distinguished between observations with incidence angle smaller and greater than 30°. The plot in Figure 12a shows the temporal evolution of the slopes for the 12 narrow-band filters. All filters followed a smooth curve with a higher dispersion at shorter wavelengths, forming a shallow depression with the minimum on the martian aphelion, which was expected due to the larger distance from the Sun. The maximum will occur at the perihelion (sol 475). Notably, around sol 315 a major dust event raised a significant amount of dust in the atmosphere and on the cal-targets, causing a sudden drop in the irradiance. Since then, the irradiance kept increasing at levels lower than those before the event.

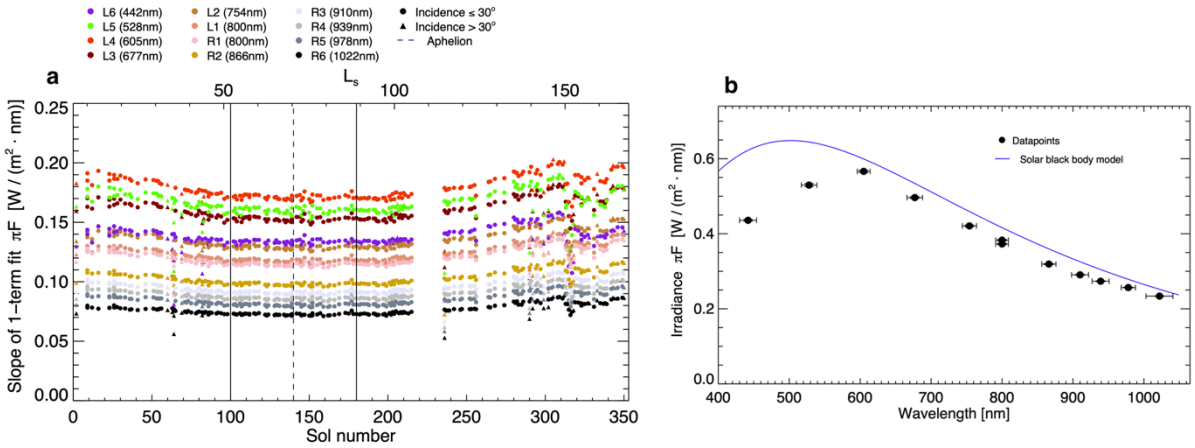

Figure 12. (a) Time evolution of the solar irradiance from landing to sol 350, in terms of slopes of the one-term linear fits between radiance and reflectance of the cal-targets. The colors represent the different narrow-band filters of Mastcam-Z. The blue dashed line is the martian aphelion. (b) Solar irradiance spectrum at the martian aphelion. The black points are the sample spectrum of solar irradiance obtained as the average of the slopes in each filter, while the blue solid curve is a model black body curve for the Sun (T=5775 K) as seen from Mars. The two solid vertical lines in the plot on the left (sol 100 and sol 180) enclose the interval of the slopes used to make the spectrum in (b).

The subsequent step of the analysis was the extraction of the spectral irradiance of the Sun. For each narrow-band filter, we computed the average of the slopes over the time range which showed the most flatness of the curves. This was centered on the aphelion (sol 140) with a maximum margin of 40 sols in each time direction (i.e., from sol 100 to 180). The resulting spectrum, sampled in the 11 wavelengths, is reported in the Figure 12b together with a model black body spectrum of the Sun (T = 5775 K) as reference. The data points match the model spectrum quite well for longer wavelengths but fall below at shorter wavelengths as expected due to absorption by dust in the Martian atmosphere.

1. **Dust Assessment and Properties**

Some insights on the martian dust within the rover site can be retrieved from Mastcam-Z images of the cal-targets. These include the deposition of dust and other materials on the cal-targets surfaces, the magnetic properties of the dust on the magnet rings, as well as the evolving atmospheric dust content.

1. **Deposition of Material on the Calibration Targets**

During the first 350 sols of Perseverance on Mars, we observed variability in the dust patterns on the cal-target surfaces and on the deck in the immediate vicinity of the primary target. Sol after sol, layers of airfall dust and larger sand grains were transported by the wind, deposited on those flat areas and

were displaced or even cleaned out by wind events and the motion of the rover. In order to monitor the dust settlement and displacement more efficiently, we realized a movie sequence of all the radiance-calibrated RGB images of the cal-targets acquired by the left eye of Mastcam-Z from landing to sol 350, suitably aligned by an algorithm to minimize shifts and distortions between the frames. The movie is available in the supplementary material (movie S2). From the movie, the deposition of dust and sand was very modest up to sol 86, when several small grains were transported on the deck. Between sols 124 and 138 there was a more intense wind activity, which continuously displaced larger sand grains and swept away the finer dust. Around sols 166 and 169 fine grains deposited on the deck, the grayscale rings and the secondary horizontal target. From sol 280 to 299 more fine grains deposited on the grayscale rings, while the larger sand grains were translated several times by few millimeters. On sol 314 a major dust event struck, bringing a large amount of dust and fine sand grains on all the surfaces of the deck and the cal-targets, that was more perceivable from sol 316. A considerable fraction of this dust was swept off of all these surfaces first between sols 327 and 333, and then on sols 349 and 350, when the deck and the grayscale rings appear quite clean and on the secondary target the dust is concentrated along the side between the horizontal and the vertical rows.

Figure 13 displays the distribution of a significant dust layer on sol 318, which formed during the major dust event that struck from sol 314. This fine dust, recognizable from the darker brown tone in the color image on the left, is more discernible in the corresponding decorrelation stretch (DCS) in the L2, L5 and L6 filters on the right, a technique that enhances color differences in an image (Gillespie *et al.*, 1986). Within the DCS image, the dust appeared as a purple coating on the deck around the primary target, on the grayscale rings and on the secondary horizontal tiles.

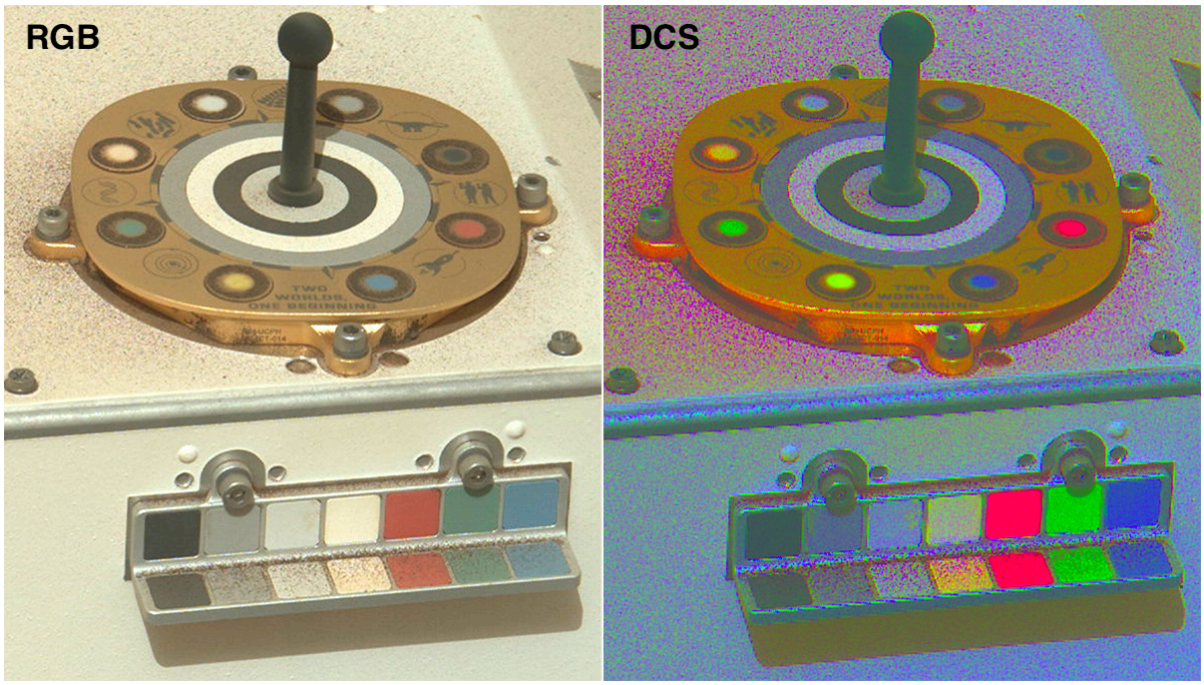

Figure 13. Highlight of the airfall dust on the cal-targets and the rover deck on sol 318, as result of the dust event that started on sol 314. The left image is an RGB shot by the left eye of Mastcam-Z on sol 318 at 48 mm zoom (seq. ZCAM03014), while the image on the right is the outcome of a decorrelation stretch (DCS) performed on the left image. The DCS was obtained using the L2 (754 nm), L5 (528 nm) and L6 (442 nm) filters for the Red, Green and Blue channels, respectively. Image-ID: ZL0_0318_0695174407_428ECM_N0090000ZCAM03014_048085J.

Large sand grains appeared frequently in the cal-target frames, with a characteristic dark color. These grains were able to persist for several sols on the deck around the cal-targets, since a strong drag force of the wind or vibrations due to the rover's drive are required to move such massive and large grains. Figure 14 shows four examples of such grains on the deck around the primary target imaged by Mastcam-Z on sols 23 and 302, with a zoom-in on one of those grains (Fig. 14c).

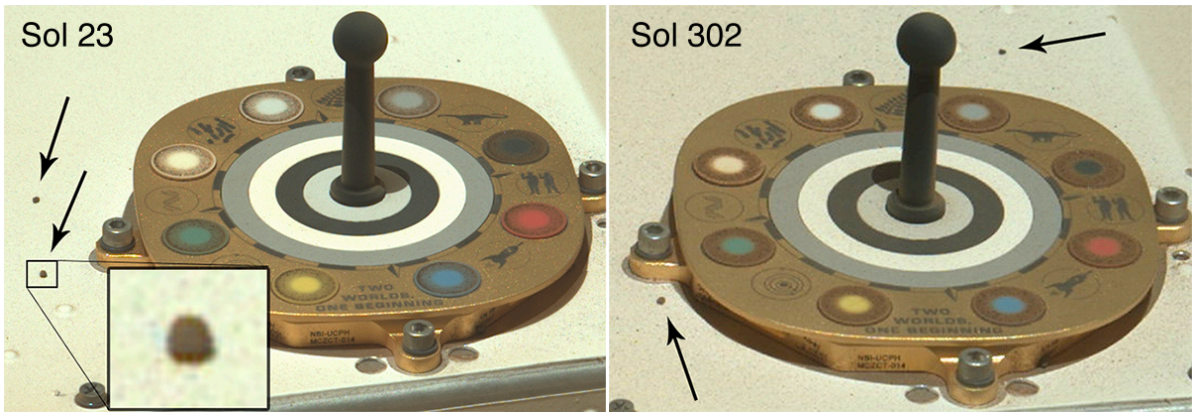

Figure 14. Primary target imaged by the left eye of Mastcam-Z (a) on sol 23 at 100 mm focal length (seq. ZCAM03014) and (b) on sol 302 at 48 mm focal length (seq. ZCAM03014) with the presence of large sand grains indicated by arrows. (c) One of the grains in the sol 23 image is magnified for better display. Image-IDs: (a) ZLF_0023_0668983099_596FDR_N0030770ZCAM03003_1000LMJ, (b) ZL0_0302_0693748246_223ECM_N0090000ZCAM03014_048085J.

However, the regions which experienced the greatest accumulation of dust were the magnet rings of the primary target. As anticipated in section 2, the aim of the underlying magnets was to attract magnetic dust on the external rings of the round patches. The visible condition of these rings was shown in Figure 6, where a small quantity of dust already deposited during the first 23 sols and the thickness of the dust layer was quite considerable at the end of the period under examination, in which the color of the patches was almost completely invisible under the dark red/brown coating (Fig. 6d). We extracted the reflectance factor values of the magnet rings from several sols, where the ROIs of the magnet rings were selected with the template of Figure 4. Four spectra of the magnet rings are shown in Figure 15 for sols 12, 129, 265 and 346 for the eight color and grayscale materials. Generally, the dust layers decreased the reflectance of the brighter patches and raised that of the darker patches, bringing their appearance to a convergence with a reduction of the contrast and reddening. At the end of the time range under exam (Figure 15d), the magnet rings were almost coincident at shorter wavelengths, but showed a slight separation in the near infrared, suggesting that in that range the dust was less optically thick to the color patches underneath.

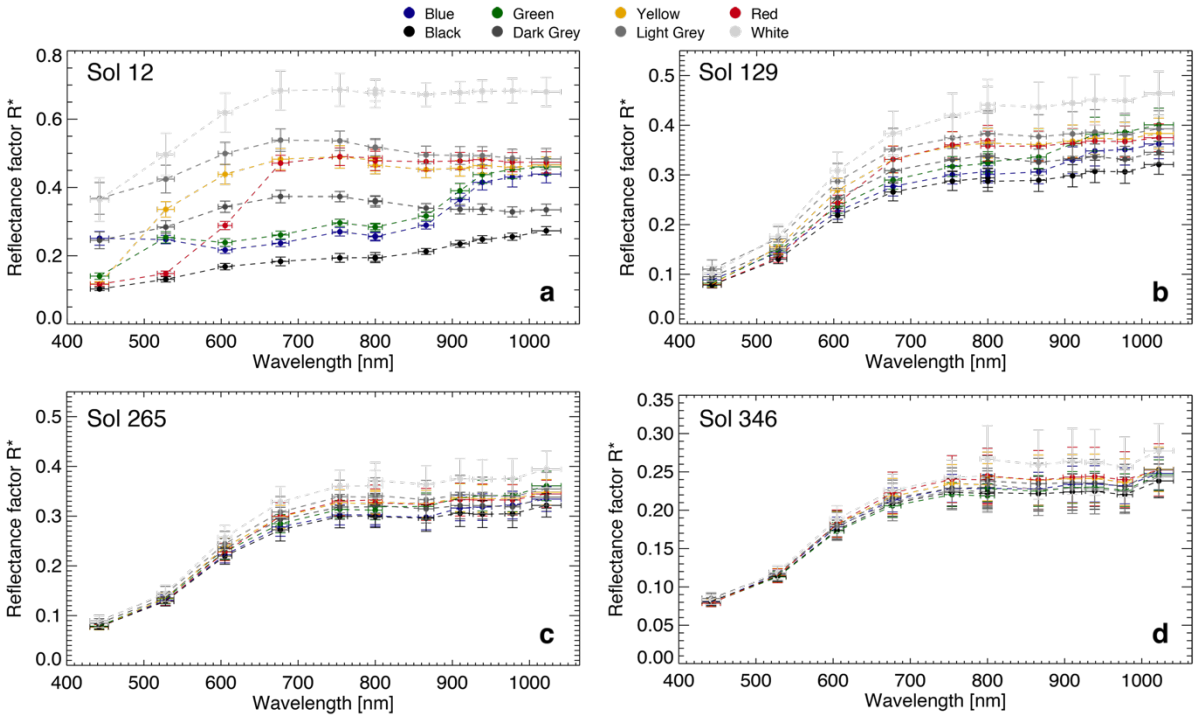

Figure 15. Spectra of the magnet rings of the primary calibration target in four different moments of the mission: (a) sol 12, (b) 129, (c) 265, (d) 346. Each color corresponds to a different color or grayscale material. The scales of reflectance factor for sols 129, 265 and 346 have been adapted to the plot size for better display.

1. **Direct and Diffuse Sunlight on the Grayscale Rings**

Suspended dust is one of the main sources of diffusion of sunlight within the thin martian atmosphere. This phenomenon affects the measured radiance of the observed targets because the surfaces directly illuminated by the Sun will receive the sum of direct sunlight and diffuse light, while the shaded regions will receive only light from the diffuse component. The diffuse light and the presence of dust in the atmosphere can be evaluated using the direct fraction of sunlight F_d (Kinch *et al.*, 2007), defined as follows:

$$F_d = \frac{\mathrm{RAD_{illum}} - \mathrm{RAD_{shad}}}{\mathrm{RAD_{illum}}} \ , \quad (3)$$

where $\mathrm{RAD_{illum}}$ and $\mathrm{RAD_{shad}}$ are the measured radiances of illuminated regions and shadowed regions, respectively. On the cal-targets, the illuminated regions used for this calculation are the four grayscale rings exposed to the sunlight,

while the shadowed regions are the four small portions of the grayscale rings under the shadow of the central gnomon. For each ring for which the shadow was selected and the radiance measured, a value of F_d was computed using (3) and then the average was retrieved over the rings. Changes in F_d in time usually indicate an increase or decrease of the light diffusion in the atmosphere and hence, in turn, a change in the amount of airborne dust. The trends of F_d are often correlated with the detections of the atmospheric optical depth τ, which describes the attenuation of the solar radiation penetrating the atmosphere. Visible optical depth was measured via direct solar images taken by Mastcam-Z using solar filters (Bell *et al.,* 2021, 2022). Solar images were taken with an RGB filter and with an 880 nm filter, the latter of which was used here. Optical depth varies by <5% across the Mastcam-Z wavelength range (Lemmon *et al.*, 2019). Solar images were reduced to optical depths following the procedure of Lemmon *et al.* (2015), simplified due to the lack of need for a temperature correction and the lack of observed dust on the optics so far.

Figure 16 represents the comparison between the time trends of F_d in four different filters (L6, L4, R2 and R6) and τ_I, the latter being observed at 880 nm. The direct fraction F_d and the optical depth are expected to vary in an inverse fashion, with increases in F_d corresponding to drops in the optical depth and vice-versa. The time range from landing to the solar conjunction (sol 217) was characterized by a fairly stable, low optical depth. This is shown in Figure 16 by a slight depression around the martian aphelion counterbalanced by the local peak of F_d, which reaches 0.81 at 605 nm. After conjunction (from sol 236) a first decrease in τ_I was followed by a series of spikes between sol 285 and 305. Subsequently, the aforementioned major dust event occurred on sols 314-316, with a corresponding drop in F_d to 0.41 at 605 nm. In the aftermath of the dust event and up to sol 350, F_d remained stable and low in all filters, suggesting that the dust raised and transported by the wind persisted in the atmosphere. The values of F_d represented by triangles in the F_d plot of Figure 16 that appear considerably lower than the general trend (sols 64, 82, 83 and 236) are cal-target observations made with $i > 60^\circ$.

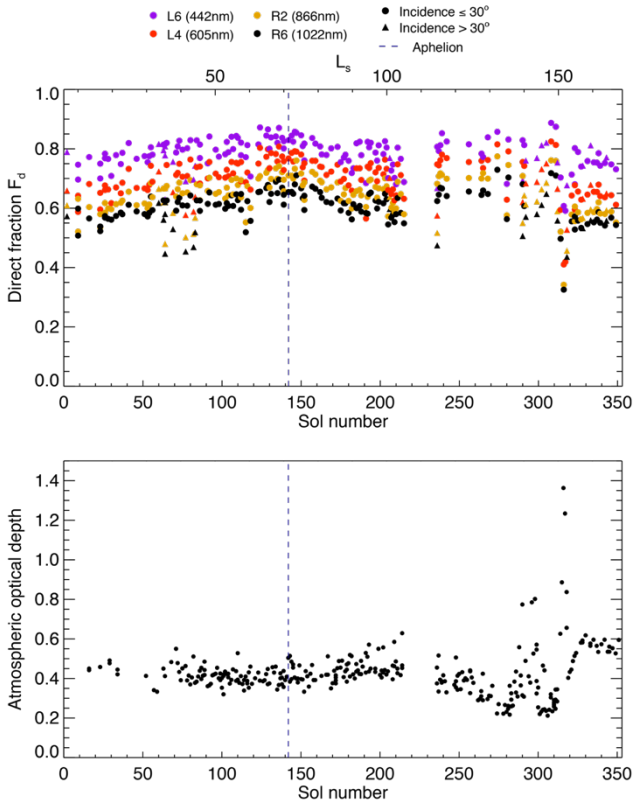

Figure 16. Top panel: time evolution of the direct fraction F_d of sunlight on the grayscale rings, as computed using equation 3, for the L6, L4, R2 and R6 filters. Bottom panel: time evolution of the atmospheric optical depth τ_I measured at 800nm through Mastcam-Z observations of the Sun.

1. **The two-term linear fits**

Since the landing of Perseverance, the linear fits employed for Mastcam-Z calibration have regularly been performed involving only one multiplicative term. This is a consequence of the fact that the radiance and the IOF reflectance of the clean spots of the cal-targets are expected to be directly proportional and lie on a line passing through the origin, and the conversion factor is the solar irradiance. However, our data suggested that a second term, an additive offset, might provide a better consistency between the measured data and the fits. Therefore, we tested a two-term linear fit model to all the radiance-reflectance sets from the RC-files in order to study how these fits changed within the first 350 sols and for comparison with the one-term fits. Figure 17 is a collection of radiance-versus-reflectance plots from different sols and filters showing both models (one- and two-term fits) and reporting the corresponding numerical values. Similar to the one-term fits, the white clean spot was excluded from the

computation of the fits, due to its misbehavior (see sect. 4.6). The fits with the offset appeared to be systematically less steep than the one-term counterparts and represented better the datapoints. The average reduced chi-squared $\chi^2_{\rm red}$ among all narrow-band filters was 2.52, with a roughly decreasing tendency from the shorter wavelengths to the near infrared filters, ranged between 1.43 in R5 (978 nm) and 4.71 in L4 (605 nm).

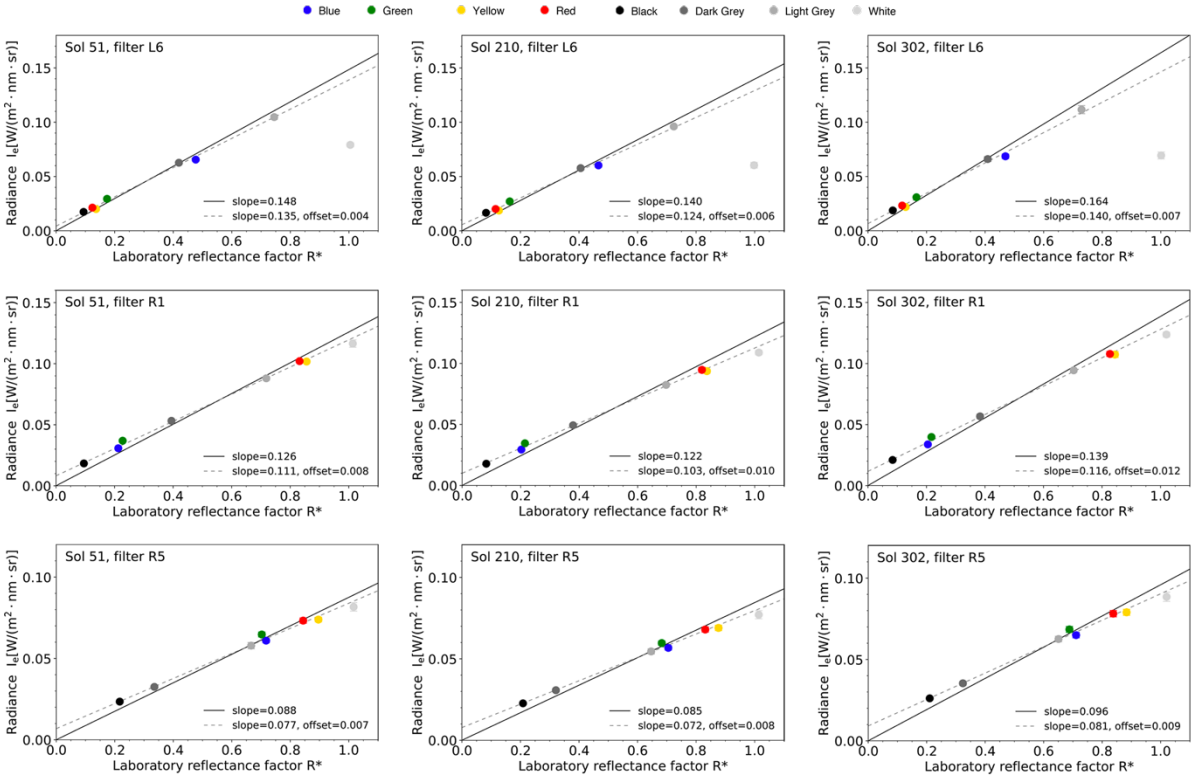

Figure 17. Plots of measured radiance-vs-model reflectance factor for 3 sols (51, 210 and 302) in 3 filters (L6, R1 and R5), showing the related one-term fit model (solid line) and the two-term fit model (dashed line). The values of the slopes and offset are reported for both models in each box.

The slightly greater flatness of the two-term fits that came out of the slope computation also resulted from the relative difference between the slopes in the two models. We quantify this relative difference $[(\text{slope}_{\text{two\_term}} - \text{slope}_{\text{one\_term}})/\text{slope}_{\text{one\_term}}]$ in Figure 18a for four filters (L6, L3, R2, R6). The datapoints at very low values on sol 9 and 23 were due to a low resolution (26 mm and 34 mm, respectively). If we exclude these two observations and those after sol 314, that were strongly perturbed by the dust event, the differences were negative and slightly increasing in absolute value with time. The difference in filter L6 (442 nm, purple circles) had a net

decrease from -0.09 to -0.12 (-35%), while R6 (1022 nm, black circles) went from -0.17 to -0.20 (-13%). All the other filters followed similar trend, with rates between -15% and -28%. In addition, the relative differences in slopes did not follow any linear dependency on wavelength. The plot of Figure 18b shows the averages of the relative differences for each filter over the sol range 100-180 (across the martian aphelion, highlighted by the two vertical solid lines in the left plot). All the points are included between -0.2 and -0.07, with L6 being the highest and R6 the lowest. The spectrum of the relative difference is characterized by a decrease from -0.09 in L6 to -0.15 in L4 (442 nm to 605 nm), followed by a rough slight increase up to -0.14 in R5 (978 nm) and a drop to -0.19 in R6.

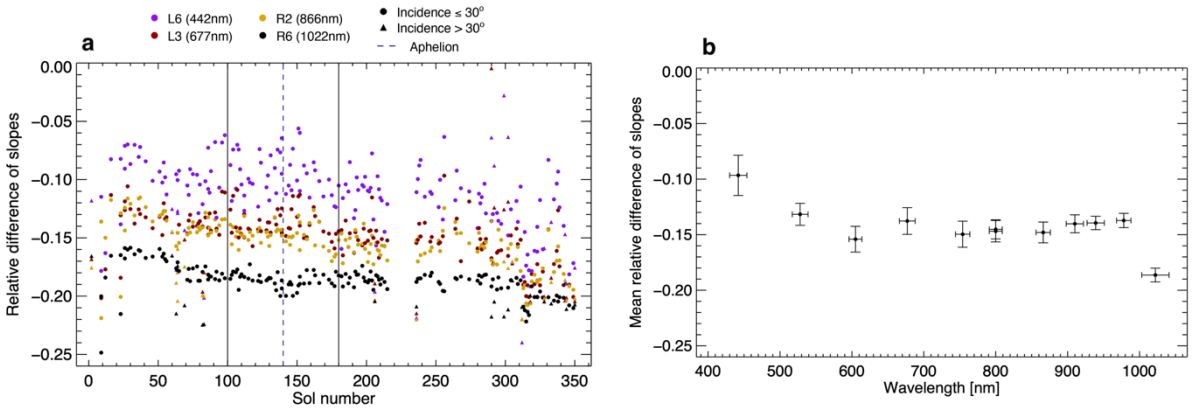

Figure 18. (a) Time evolution of the relative difference between the slopes of the two- and one-term fits for four narrow-band filters. Each color corresponds to a different filter. The relative difference is computed as $[(\text{slope}_{two\_term} - \text{slope}_{one\_term})/\text{slope}_{one\_term}]$. The circles are observations with $i \leq 30°$, the triangles are $i > 30°$. The vertical dashed line is the martian aphelion. (b) Average of the relative difference of slopes for all 12 narrow-band filters, over the range from sol 100 to 180 (corresponding to the two vertical solid lines in the left plot).

The offsets for all the 2-term fits over time from landing to sol 350 are represented in Figure 19 for the primary clean spots, the grayscale rings, and the secondary horizontal tiles. The white patch was excluded from the computation of the fits for the primary clean spots and the secondary horizontal target, but not for the grayscale rings, since it was not observed there. The offsets are calculated in radiance units, that we converted to units of IOF for easier comparison filter-to-filter and sol-to-sol. The offset values are roughly wavelength dependent, increasing with increasing wavelength. Most filters fall fairly close in a tight band between 0.05 and 0.1 while the shortest and longest wavelengths fall outside this range. The clean spots (Fig. 19a) and secondary horizontal target (Fig. 19c) are quite similar, while the grayscale rings (Fig. 19b) are characterized by a more dramatic divergence in the near infrared filters (R4-R6,

from 900 nm to 1000 nm), though also in this case the L6 is consistently well below the other filters. The average increase of the offsets for the grayscale rings was 14% and for the secondary horizontal target 25%, on average. In particular, for the secondary horizontal target the increase rate became flatter towards the longer wavelengths (from 56% in L6 to 7.7% in R6). The grayscale rings present a more random such distribution, with the filters R4-R6 (from 900 nm to 1000 nm) following a slight decrease (-8% in R6). The offsets are quite stable in time showing a limited increase over the 350 sols. Figure 19d shows the offsets of the clean spots as function of the wavelengths of the 12 narrow-band filters, where the offsets in each filter have been averaged over the first 100 sols (blue circles) and the last 100 sols (red circles) considered in our analysis (sols 0 to 350). The spectral shape of the offsets showed a smooth trend with first increase between L6 and L2 (442 nm and 754 nm, respectively), followed by a slight decrease and a final increment from R2 (866 nm) to R6 (1022 nm). In addition, the mean offsets in the 250-350 sol interval were 14% higher than those in the first 100 sols of the mission, with a minimum increase in the near infrared (6.3% in R6) and larger increase at shorter wavelengths (20.7% in L6).

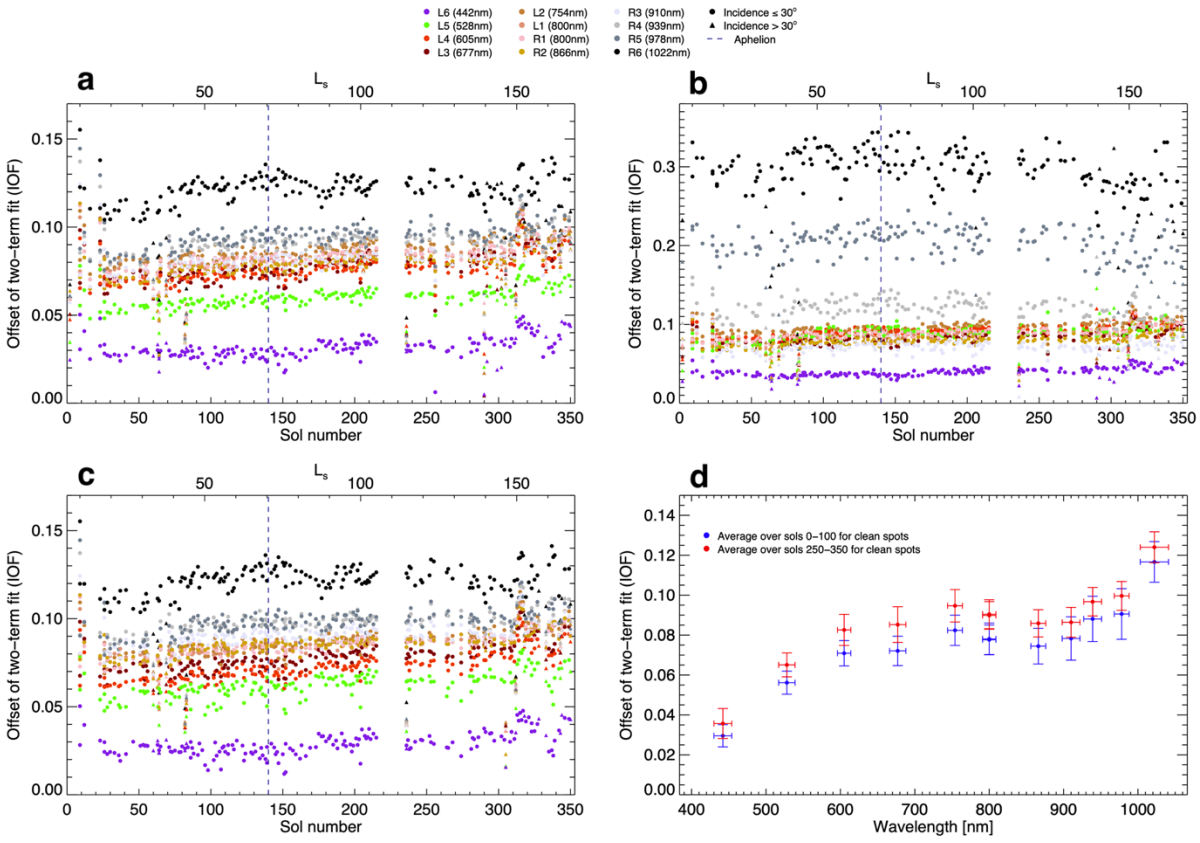

Figure 19. Time evolutions of the two-term linear fit offsets within the first 350

sols on Mars for (a) primary clean spots, (b) grayscale rings and (c) secondary horizontal patches. Each color corresponds to a different narrow-band filter. The dashed vertical line is the martian aphelion. (d) Offsets of the clean spots averaged over the first 100 sols of mission (blue circles) and on the last 100 sols considered in this work (sols 250-350, red circles), represented as function of the wavelength of the corresponding narrow-band filters.

1. **The yellowing of the AluWhite98**

One of the prominent discoveries related to the cal-targets was the "yellowing effect" of the AluWhite98 material. The impact of this problem in time was documented since landing through the progressive yellowing of the white patches in the color images, and the advancing decrease of the corresponding measured short-wavelength radiance, which reflected in the linear fits (Figure 10) and hence, the cal-targets spectra (Figure 11). Therefore, the primary white patch was excluded from the IOF calibration procedure, which always relied on the other seven clean spots. Figure 20 presents a close-up on the primary white and light gray patches in four different sols. The gradual deterioration of the white color is evident as time passed, especially if compared to the light gray and to the white grayscale ring, which did not show any change. Both secondary AluWhite98 tiles were also affected. In addition, the issue was more emphasized at shorter wavelengths (L6, L5 and L4) and was gradually fainter and imperceptible towards the near infrared. Curiously, the white ring, which is manufactured from the same material, was unaffected or only affected to a very limited degree.

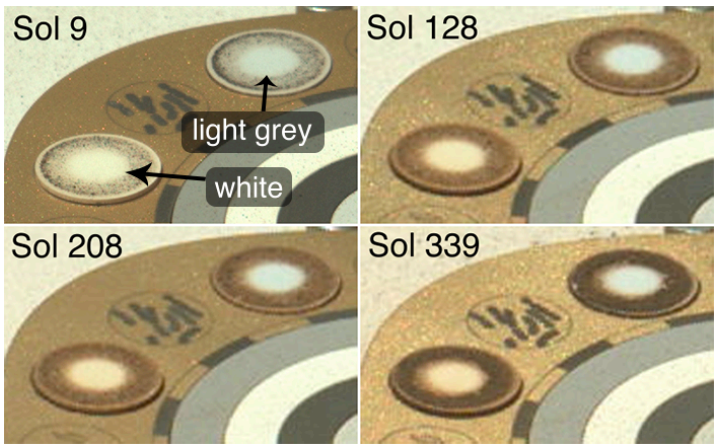

Figure 20. Visual juxtaposition of 4 close-ups of the primary white and light gray patches of the cal-targets imaged by the left eye of Mastcam-Z on sol 9, 128, 208 and 339 to highlight the progressive visual yellowing of the AluWhite98. In each image, the white patch is on the left, the light gray on the right. Image-IDs: (a) ZLF_0009_0667741621_074FDR_N0020000ZCAM03000_1100LMJ, (b) ZR0_0128_0678304502_223ECM_N0041860ZCAM03014_048085J01, (c) ZR0_0208_0685400431_053ECM_N0071836ZCAM03014_048085J01, (d)

ZR0_0339_0697031476_144ECM_N0090276ZCAM03014_048085J01.

To have a better overview on the spectral dependency of the yellowing, the time evolution of the ratio between the measured and the expected IOF reflectance is reported in Figure 21 for the primary white patch, the primary light gray patch, the white grayscale ring, and the white secondary horizontal tile.

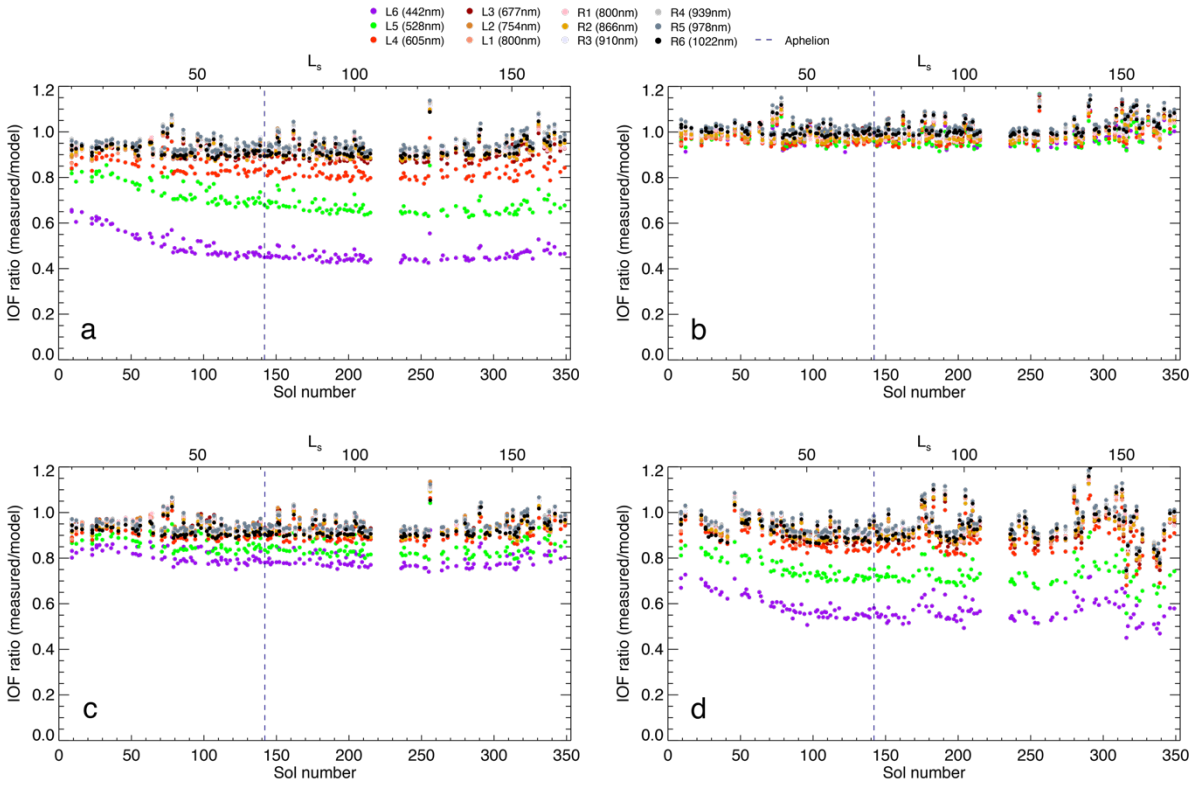

Figure 21. Ratio between the measured IOF and the model IOF values of (a) the primary white central spot, (b) the light gray central spot, (c) the white grayscale ring and (d) the secondary white horizontal patch. Only datapoints with incidence angles <30° are plotted to avoid those affected by disturbances by diffuse light and scattering on the target. The colors of the points are the same for the four plots and represent the narrow-band filters. The vertical dashed line is the martian aphelion.

For the primary white patch (Fig. 21a), the points were systematically just below 1 for all filters spanning the range between 677nm and 1022nm, while filters L4 (605nm), L5 (528nm) and L6 (442nm) displayed progressively lower values. These three filters followed a similar trend: a first interval, from landing to sol 100, characterized by a linear and faster decrease, followed by a flatter decline which lasted at least until the solar conjunction of sols 217-235. After conjunc-

tion, they tended to be overall more stable (L6 seemed to increase slightly) up to the period of the major dust event of sol 315. There was not a clear relationship with the solar aphelion. For reference, Fig. 21b shows unchanging ratios for the light gray primary patch. This material did not exhibit any significant deviation from the unit ratio before the dust event. Although manufactured from the same material as the other white patches, the white primary ring was not or only very slightly influenced by the yellowing effect (Fig. 21c).

1. **Discussion**

In this section we discuss the performance of the Mastcam-Z radiometric calibration target in light of the results presented in section 4. Principally, we want to evaluate the performance of the cal-targets over the first 350 sols on Mars and the model used to generate the reflectance-calibrated products. In addition, we display a basic assessment of the dust on the cal-targets and its effect on the diffuse light. Eventually, we describe the tests that were aimed at understanding the visual and spectral deterioration of the AluWhite98 material.

1. **The cal-targets performance and the linear fit model for IOF calibration**

The performance of Mastcam-Z calibration targets can be assessed from the results reported in sections 4.2 and 4.3, and the visual inspection of the regions involved in the IOF calibration process within the color images (section 4.1). The plots of Figure 10 show a limited dispersion of the data from the fit lines (except for the white), where this dispersion was quantified as a relative error on the slopes of less than 3.5% on average. This small deviation indicates that the cal-targets were successful in achieving their main goal, especially thanks to their design and the inclusion of the permanent magnets. The number of clean spots, higher than in the previous missions, considerably reduced the impact of the exclusion of one of those regions (the AluWhite98) from calibration, thanks to the other seven regions. The presence of the hollow magnets below the primary patches but not in the secondary target was a useful way to visually infer the accumulation of airfall dust on the surfaces. The magnet rings, as expected, were the first regions to be covered in dust, as shown in Figures 6 and 15. We should also consider the action of the wind, which contributed to a frequent and efficient deposition and cleaning from dust on the cal-targets (e.g., on sols 327 and 349, as shown in the movie S2). These effects on the clean spots were critical for the radiometric calibration, because they ensured minimal dust disturbance of the clean spots' radiances when the linear fits were made with the corresponding laboratory reflectances (Fig. 10). As a consequence, the datapoints in those plots were well described by the one-term fit model, which was expected by the theory (eqn. (2)). The 'cleanliness' of the clean spots due to the magnets and the wind was adequately maintained in time, as suggested by the solar irradiance time series (Fig. 12a). Indeed, the irradiance F followed a quite stable and smooth trend in all filters up to the dust event of sols 314-316 that caused a significant unsettlement in images and radiance values, but that did not compromise the cal-targets or their surfaces. Further

proof of the effectiveness of the clean spot-magnet ring system was the solar irradiance spectrum at the aphelion (Fig. 12b), which is consistent with a solar black body model allowing for some atmospheric absorption, particularly at short wavelengths.

As mentioned in section 4.2 and fully treated in section 4.5, though the one-term linear fits characterize well the radiance-reflectance datapoints, we noticed a small offset in the distribution of the datapoints with respect to the straight line passing through the origin. The testing of a two-term model for the linear fits gave better statistical outcomes. Over the whole sets of radiance-reflectance data, the one-term model yielded a reduced χ^2 between 10.7 and 34.4, the two-term yielded values between 1.43 and 4.71. The exact nature of this offset is not yet known. It might be due to some computational source, such as residuals from the radiance-calibration process when the corrections (bias frames, flat fields, etc.) are applied to the raw images, or slight discrepancies in the reflectance model that is employed to give an estimate of the expected reflectance of each clean spot at any illumination geometry. The presence of dust on the surfaces would also tend – to first order – to result in a straight line with an offset. The slowly increasing trend of the offset in all the narrow-band filters might indicate a dust-related origin. This may imply that a small fraction of weakly or even non-magnetic airfall dust (not attracted or repelled by the magnets) gradually deposited within the clean spots and adhered electrostatically, such that it could not be swept by. The fact that the offsets are largest at long wavelengths is not consistent with expectations for the effect of dust however, which would be expected to be more pronounced at the shortest wavelengths. This might not only be gradual accumulation of airborne dust but could also be dust and sand that was raised by the rockets of the skycrane during landing. Deeper investigation is required to fully understand the origin and the nature of this offset.

1. **Preliminary dust assessment**

Martian dust was the main component that interacted with the cal-targets and that we could observe both directly (by deposition on the surfaces from which we measured the radiance and their surroundings) and indirectly (by analyzing its effect on the light that illuminated the cal-targets). As shown in the irradiance time series in Figure 12a, which only refer to the clean spots (expected to be the cleanest regions of the cal-targets), in absence of larger events dust never had a significant impact on the cal-targets or their ability to correctly perform the IOF calibration. On the other hand, as mentioned above, the frames of the movie S2 express a frequent change in the material that accumulated on the deck of the rover. We could recognize patterns of fine dust layers, which were more evident on the deck and on the bright materials, due to the higher light/dark-toned contrast, and single larger grains of sand or regolith raised from the surface, which in some cases moved for few mm or cm across two consecutive sols. Whereas the peripheral regions of the primary target were likely ruled by the magnetic field of the magnets (in particular the round patches and the

outermost grayscale rings), which produced an optically thick buildup of dark reddish dust on the magnet rings, the variations in all the other regions were probably controlled by wind (e.g., several dust devils were observed by Mastcam-Z in the rover site; Newman *et al.*, 2022) and possibly aided by vibrations caused by the motion of the rover, which traveled almost 4 km in the first 350 sols. This fine dust not only deposited on horizontal surfaces, but also adhered to vertical sides, such as the lower part of the golden base of the primary target where the magnetic field from the permanent magnets is prominent and on the cylindrical structure of the gnomon (the reddish dust coating is just perceivable on its boundaries in Fig. 6).

The model of the direct fraction of sunlight on the illuminated and shaded grayscale rings was a powerful method to follow the presence of dust suspended within the martian atmosphere. The two time series shown in Figure 16 display a roughly inverse correlation in the sense that F_d rises when τ_I falls and vice-versa. This can be interpreted in a way that a growth in the density of dust in the atmosphere leads to an increase of the optical depth measured from Mastcam-Z images and increase scattering of sunlight, leading to a decrease in F_d. In addition, F_d and τ_I show a shallow local maximum and minimum, respectively, around the martian aphelion. The correlation can be recognized after the solar conjunction, when stronger perturbations caused a higher variability in F_d and τ_I, and upon the major dust event from sol 314.

The spectra of dust accumulated on the magnet rings (Figure 15d) are consistent with previous observations of martian dust attracted to permanent magnets (e.g., Madsen *et al.*, 2009). The dust is brownish-red with very low reflectance factor at ultraviolet and blue wavelength, a characteristic rise from green to red consistent with the presence of ferric iron and higher reflectance factors in the red and infrared. Overall, though, the spectrum is darker than a typical spectrum of martian bright dust, again consistent with expectations for magnetically-attracted material that can be expected to be richer in magnetite and with a larger average grain size (Kinch *et al.*, 2006).

1. **The AluWhite98**

We have not yet been able to identify a root cause of the observed yellowing of the white patches of the cal-targets. The white material is different (AluWhite98 manufactured by Avian Technologies) from the seven other materials (glazed ceramic material manufactured by Lucideon) (Kinch *et al.*, 2020). This explains why this effect was only observed in the white patches but it remains enigmatic why the white ring was not or almost not affected. One hypothesis suggested that a possible cause was the different type of epoxy adhesive employed to fix on one hand the primary and secondary patches and tiles (Henkel/Loctite EA-9309NA) and on the other hand the white ring (3M-2216B/A Gray) to their supports.

Several tests of martian environment simulation were carried out on four spare AluWhite98 samples. Three of these samples were fixed onto an Aluminum

support using the two types of epoxies mentioned above, whereas the fourth was put in place without any adhesive. The samples underwent the same baking process of preparation as those currently within the cal-targets on Mars, and were treated with UV irradiation at the University of Winnipeg. However, the tests did not reproduce the visible, radiometric, and spectral outcomes of the in-flight materials. This issue therefore remains unsolved.

1. Conclusions and future work

In this work we assessed the performance of the Mastcam-Z radiometric Calibration Targets (or cal-targets; Kinch *et al.*, 2020), regularly employed to convert Mastcam-Z images (Bell *et al.*, 2021) from units of radiance to reflectance, over the first 350 sols on Mars.

The cal-targets proved to be efficient not only for calibration, but also to retrieve information on the environment and the dust dynamics within Jezero crater. The design of the regions of interest for calibration, surrounded by strongly magnetized hollow cylindrical magnets, allowed accurate measurements of the local radiances (Hayes *et al.*, 2020) involving low disturbance due to dust, which was mostly attracted or repelled by the magnets, or deposited and cleaned by the wind. Linear fits between model reflectances and observed radiances are of good quality with only limited dispersion of data points around the fit line. A continuous monitoring of the linear fits, as well as their slopes (proportional to the instantaneous local solar irradiance), will ensure a correct application of the reflectance calibration procedure in the future, as significant natural events (such as e.g., the major dust event of sols 314-316) can directly affect the atmospheric optical thickness and the cal-targets materials, hence perturbing the stability of the calibration process. This includes the implementation of a dust model, which was already performed in the MER mission (Kinch *et al.*, 2007). Due to the satisfying results from Mastcam-Z cal-targets within the first 350 sols, we do not contemplate the urgency of a dust model.

We did observe that the linear fits could consistently be improved by the inclusion of a slight offset term. The origin of this offset is not yet understood but plausible hypotheses include residuals of the radiance calibration, imperfections of the reflectance model, or dust, or some combination of the three.

Finally, the yellowing effect of the AluWhite98 patches of the primary and secondary cal-targets could not yet be reproduced by experiments and therefore for now remain an unexplained phenomenon. Determining the physical trigger of this effect could help establish the starting point and provide a useful reference in the design of the new calibration targets for the cameras of coming planetary missions.

Acknowledgements

M. Merusi is supported by the European Union's Horizon 2020 research and innovation programme under the Marie Skłodowska-Curie grant agreement No 801199. Support from the Carlsberg Foundation, grant CF16-0981,

CF17-0979, and CF19-0023 are gratefully acknowledged. This support made it possible to build the cal-targets and to allow Danish team members to participate in a number of team meetings. J.R. Johnson is supported by ASU Contract 151112, 15-707. E.A. Cloutis thanks the Canadian Space Agency, the Natural Sciences and Engineering Research Council of Canada, and the University of Winnipeg for their funding support. M.T. Lemmon is supported by contract 15-712 from Arizona State University and 1607215 from Caltech-JPL. O. Gasnault's work with SuperCam on Perseverance was supported by CNES.

Open Research (availability statement)

All image data presented here from the Mastcam-Z, WATSON and SuperCam instruments are available through the Planetary Data System Imaging Node (https://pds-imaging.jpl.nasa.gov/portal/mars2020_mission.html) and Geo-Sciences Node (https://pds-geosciences.wustl.edu/missions/mars2020/), under the Mars 2020 Mission.

SuperCam RMI and WATSON imaging products may be found within the Img_Ops data collection hosted within the PDS Cartography and Imaging Sciences Node at the Jet Propulsion Laboratory (https://pds-imaging.jpl.nasa.gov/), under the Mars 2020 Mission.

References

Balaram, J., Aung, M. & Golombek, M.P. (2021). The Ingenuity Helicopter on the Perseverance Rover. *Space Sci. Rev.*, **217**, 56. https://doi.org/10.1007/s11214-021-00815-w.

Bell, J. F. III *et al.* (2003). Mars Exploration Rover Athena Panoramic Camera (Pancam) investigation. *J. Geophys. Res.*, **108**(E12), 8063. https://doi.org/10.1029/2003JE002070.

Bell, J. F. III *et al.* (2006), In-flight calibration and performance of the Mars Exploration Rover Panoramic Camera (Pancam) instruments, *J. Geophys. Res.*, **111**, E02S03, https://doi.org/10.1029/2005JE002444.

Bell, J. F., III *et al.* (2017). The Mars Science Laboratory Curiosity rover Mastcam instruments: Preflight and in-flight calibration, validation, and data archiving. *Earth and Space Science*, **4**, 396–452, https://doi.org/10.1002/2016EA000219.

Bell, J.F., III *et al.* (2021). The Mars 2020 Perseverance Rover Mast Camera Zoom (Mastcam-Z) Multispectral, Stereoscopic Imaging Investigation. *Space Sci. Rev.*, **217**, 24. https://doi.org/10.1007/s11214-020-00755-x.

Bell, J.F., III *et al.* (2022). Geological and Meteorological Imaging Results from the Mars 2020 Perseverance Rover in Jezero Crater. Under review.

Bhartia, R. *et al.* (2021). Perseverance's Scanning Habitable Environments with

Raman and Luminescence for Organics and Chemicals (SHERLOC) Investigation. *Space Sci. Rev.*, **217**, 58. https://doi.org/10.1007/s11214-021-00812-z.

Buz, J. *et al.* (2019). Photometric characterization of Lucideon and Avian Technologies color

standards including application for calibration of the Mastcam-Z instrument on the Mars 2020 rover. *Opt. Eng.*, **58**(2), 027108. https://doi.org/10.1117/1.OE.58.2.027108.

Farley, K.A. *et al.* (2020). Mars 2020 Mission Overview. *Space Sci. Rev.*, **216**, 142. https://doi.org/10.1007/s11214-020-00762-y.

Garczynski, B. *et al.* (2022). Evidence of alteration on the Jezero crater floor: A Mastcam-Z multispectral analysis. This issue.

Gillespie, A.R. *et al.* (1986). Color enhancement of highly correlated images. I. Decorrelation and HIS contrast stretches. *Remote Sens. Environ.*, **20**, 3, 209-235. https://doi.org/10.1016/0034-4257(86)90044-1.

Hayes, A.G. *et al.* (2021). Pre-Flight Calibration of the Mars 2020 Rover Mastcam Zoom (Mastcam-Z) Multispectral, Stereoscopic Imager. *Space Sci. Rev.*, **217**, 29. https://doi.org/10.1007/s11214-021-00795-x.

Horgan, B. *et al.* (2022). Mineralogy, morphology, and geological significance of the Máaz formation on the Jezero crater floor from orbit and rover observations. This issue.

Kinch, K. M., *et al.* (2006), Preliminary analysis of the MER magnetic properties experiment using a computational fluid dynamics model. *Planetary and Space Science*, **54**(1), pp 28-44, https://doi.org/10.1016/j.pss.2005.07.008.

Kinch, K. M. *et al.* (2007). Dust deposition on the Mars Exploration Rover Panoramic Camera (Pancam) calibration targets. *J. Geophys. Res.*, **112**, E06S03, https://doi.org/10.1029/2006JE002807.

Kinch, K.M. *et al.* (2020). Radiometric Calibration Targets for the Mastcam-Z Camera on the Mars 2020 Rover Mission. *Space Sci. Rev.*, **217**, 46. https://doi.org/10.1007/s11214-021-00828-5.

Lemmon, M.T. *et al.* (2015). Dust aerosol, clouds, and the atmospheric optical depth record over 5 Mars years of the Mars Exploration Rover mission. *Icarus*, **251**, 96-111. https://doi:10.1016/j.icarus.2014.03.029.

Lemmon, M. T. *et al.* (2019). Large Dust Aerosol Sizes Seen During the 2018 Martian Global Dust Event by the Curiosity Rover. *Geophysical Research Letters*, **46**, 16, 9448-9456. https://doi.org/10.1029/2019GL084407.

Lemmon, M. T. *et al.* (2022). Dust, sand, and winds within an active Martian storm in Jezero crater. This issue.

Madsen, M. B., Goetz, W., Bertelsen, P., Binau, C. S., Folkmann, F., Gunnlaugsson, H. P., *et al.* (2009). Overview of the magnetic properties

experiments on the Mars Exploration Rovers. *J. Geophys. Res.*, **114**(E6), E06S90. http://doi.org/10.1029/2008je003098

Maki, J.N. *et al.* (2020). The Mars 2020 Engineering Cameras and Microphone on the Perseverance Rover: A Next-Generation Imaging System for Mars Exploration. *Space Sci. Rev.*, **216**, 137. https://doi.org/10.1007/s11214-020-00765-9.

Mandon, L. *et al.* (2022). Reflectance of Jezero crater floor: 2. Mineralogical interpretation. This issue.

Mangold, N. *et al.* (2021). Perseverance rover reveals an ancient delta-lake system

and flood deposits at Jezero crater, Mars. *Science*, **374**, 6568, 711-717. https://doi.org/10.1126/science.abl4051.

Maurice, S. *et al.* (2021). The SuperCam Instrument Suite on the Mars 2020 Rover: Science Objectives and Mast-Unit Description. *Space Sci. Rev.*, **217**, 47. https://doi.org/10.1007/s11214-021-00807-w.

Newman, C.E *et al.* (2022). The dynamic atmospheric and aeolian environment of Jezero crater, Mars. *Science Advances*, **8**, 21. https://doi.org/10.1126/sciadv.abn3783.

Núñez, J. *et al.* (2022). Stratigraphy and Mineralogy of the Séítah formation on the floor of Jezero crater, Mars as seen with Mastcam-Z. This issue.

Rice, M. *et al.* (2022). Spectral variability of rocks and soils on the Jezero crater floor: A summary of multispectral observations from Perseverance's Mastcam-Z instrument. This issue.

Royer, C. *et al.* (2022). Reflectance of Jezero crater floor: 1. Data processing and calibration of IRS/SuperCam. This issue.

Vaughan *et al.* (2022). Regolith of the crater floor units, Jezero crater, Mars: Textures, composition, and implications for provenance. This issue.

Appendix 1 – The Radiometric Coefficient files

Here we present an example of a Radiometric Coefficient file. The following RC-file was extracted from a Mastcam-Z cal-targets image in filter L1 (800 nm) on sol 349. In this example, each line of the RC file, denoted by the initial '#', is followed by a brief explanation in brackets.

responsivity constants file: rc_ZL1___0697919834_0092982ZCAM03014_1.txt

(full-path filename of this file when it was created)

associated selection filename: Z00349_0092982ZCAM03014_048018831_FO1.sel

(full-path filename of selection file used to generate these responsivity constants)

dust correction: none

(Dust correction model used when generating responsivity constants)

outliers excluded from selections: Yes

(are ”outliers” excluded from selection regions when generating the responsivity constants...

There is currently a very strict algorithm defining outliers do be excluded. It is designed

to exclude hot pixels and the like that may be included in a selection. It is NOT meant to

be used to ignore inadvertently selected shadows or otherwise bad selections. The algorithm

operates as follows: Exclusion is determined on a per-channel basis. Histogram the pixel values

into 11 bins of equal value range from the minimum value to the maximum value. Find any outlier

bins (bins that are separated from the main cluster of values by one or more empty bins). Any

values in these outlier bins are considered to be outlier values. If the total number of

outlier values is <= 10, the mean selection value will be computed excluding these outlier

values. NOTE: If the number of outlier values is > 10, the values will not be excluded, instead

the user will be warned of this condition (which usually indicates a faulty selection), and

prompted to correct it before saving the responsivity constants.)

force fit to intercept origin: Yes

(fit line is forced to go through the point [0,0])

RC file creation time: 2022-02-12T18:26:52Z

(timestamp of when this file was created)

RC file format version: 1.1 2021-12-03

(file format version)

#

cal-target file: ZL1_0349_0697919834_098RAD_N0092982ZCAM03014_048085A01.IMG

(full-path or relative-path filename of the RAD-calibrated cal-target file used

to generate these responsivity constants)

unique sequence identifier: 00349_zcam03014_01883_001

(unique identifier of the cal-target sequence from which these responsivity constants were generated)

local true solar time: 12:22:03

(LTST of the cal-target image)

solar azimuth (rover frame): 16.5834

(solar azimuth in rover frame at time of cal-target acquisition)

solar elevation (rover frame): 64.5552

(solar elevation in rover frame at time of cal-target acquisition)

fit method: use_only_chip_centers

(method used to fit a line to the selection values. Possibilities are:

use_only_chip_centers

use_all_sunlit_regions: chip centers + sunlit rings

use_only_sunlit_rings

use_all_rings: sunlit rings + ring shadows

use_all_regions: chip centers + sunlit rings + ring shadows)

ROI names: "Blue Chip Center" "Green Chip Center" "Yellow Chip Center" "Red Chip Center" "Black Chip Center" "Dark Gray Chip Center" "Light Gray Chip Center" "White Chip Center" "Black Ring" "Dark Gray Ring" "Light Gray Ring" "White Ring" "Black Ring Shadow" "Dark Gray Ring Shadow" "Light Gray Ring Shadow" "White Ring Shadow" "Black Secondary Horizontal" "Dark Gray Secondary Horizontal" "Light Gray Secondary Horizontal" "White Secondary Horizontal" "Red Secondary Horizontal" "Green Secondary Horizontal" "Blue Secondary Horizontal" "Black Secondary Vertical" "Dark Gray Secondary Vertical" "Light Gray Secondary Vertical" "White Secondary Vertical" "Red Secondary Vertical" "Green Secondary Vertical" "Blue Secondary Vertical" "Blue Chip Outer" "Green Chip Outer" "Yellow Chip Outer" "Red Chip Outer" "Black Chip Outer" "Dark Gray Chip Outer" "Light Gray Chip Outer" "White Chip Outer" "Gnomon" "Gold" "Deck"

(names of all regions)

ROI is selected: 1 1 1 1 1 1 1 1 1 1 1 1 1 0 0 1 1 1 1 1 1 1 1 1 1 1 1 1 1 1 1 1 1 1 1 1 1 1 1 1 1

(1 if a selection exists for the corresponding named region, else 0)

ROI marked bad: 0 0 0 0 0 0 0 1 0 0 0 0 0 0 0 0 0 0 0 1 0 0 0 0 0 0 1 0 0 0 0 0 0 0 0 0 0 0 0 0 1 0 0 0

(1 if a selection for the corresponding named region has been marked bad and is

not used in the fit, else 0: the selection is allowed to be used in the fit)

ROI used in fit: 1 1 1 1 1 1 1 0 0 0 0 0 0 0 0 0 0 0 0 0 0 0 0 0 0 0 0 0 0 0 0 0 0 0 0 0 0 0 0 0 0 0 0

(1 if a selection for the corresponding named region IS used in the fit,

else 0: the selection for this region is used in the fit. Will b 0

if there is no selection for the corresponding region)

ROI radiances: 0.034506816 0.039897159 0.10376279 0.10554330 0.022406472 0.056729008 0.092273153 0.12006555 0.025852364 0.056776047 0.088735089 0.12321232 0.014249836 NaN NaN 0.044461299 0.025365373 0.058788035 0.096467562 0.12703149 0.10993537 0.042618129 0.039442647 0.014147431 0.039987970 0.069789968 0.095307037 0.079999320 0.027067456 0.024401680 0.030651826 0.030116336 0.031713024 0.032213278 0.030008674 0.031119999 0.030178478 0.033819154 0.014333907 0.058045797 0.10957697

(mean of USED values in each selected region - regions with no selection will have NaN)

ROI uncertainty: 0.0011226007 0.0011313090 0.0022528207 0.0015802836 0.0012730183 0.0015016926 0.0018925177 0.0026042091 0.0012016993 0.0013950781 0.0029164302 0.0034273181 0.0010719281 NaN NaN 0.0017609603 0.0010725553 0.0020828459 0.0047955393 0.0069235163 0.0071730291 0.0012393190 0.0010976408 0.00051002479 0.0011881783 0.0020589134 0.0032437530 0.0027616147 0.00083441847 0.00063337773 0.0025638362 0.0025350361 0.0040774076 0.0044082675 0.0027280322 0.0040012537 0.0036807128 0.0043153809 0.0029024197 0.0022435802 0.0033396325

(standard deviation of USED values in each selected region - will be NaN if no selection)

ROI count: 73 65 74 70 64 61 63 66 1517 3239 799 2239 56 0 0 100 906 882 870 872 872 870 859 1270 503 1236 1250 1250 430 1199 463 446 461 434 409 391 399 414 459 522 1732

(number of USED pixels in each selected region)

ROI incidence angle: 25.444830 65.683873 65.683873 65.683873 65.683873 65.683873 65.683873 65.683873 65.683873 25.444830 25.444830 25.444830 25.444830 25.444830 25.444830 25.444830 25.444830 25.444830 25.444830 25.444830

(Angle between the vector from the region to the sun and region surface normal for each region)

ROI emission angle: 58.310048 58.310048 58.310048 58.310048 58.310048 58.310048 58.310048 58.310048 58.310048 58.310048 58.310048 58.310048 58.310048 58.310048 58.310048 58.310048 58.310048 58.310048 55.257824 55.257824 55.257824 55.257824 55.257824 55.257824 37.229207 37.229207 37.229207 37.229207 37.229207 37.229207 58.310048 58.310048 58.310048 58.310048 58.310048 58.310048 58.310048 58.310048 58.310048 58.310048 58.310048 58.310048

(Angle between the vector from the region to the detector and the region surface normal for each region)

ROI azimuth angle: 30.933419 30.933419 30.933419 30.933419 30.933419 30.933419 30.933419 30.933419 30.933419 30.933419 30.933419 30.933419 30.933419 30.933419 30.933419 30.933419 30.933419 30.933419 31.807842 31.807842 31.807842 31.807842 31.807842 31.807842 28.666222 28.666222 28.666222 28.666222 28.666222 28.666222 30.933419 30.933419 30.933419 30.933419 30.933419 30.933419 30.933419 30.933419 30.933419 30.933419 30.933419 30.933419

(Angle in the plane of the region surface between the vector from the region to the sun

and the vector from the region to the detector)

reflectances: 0.19100898 0.20369039 0.78817137 0.77029269 0.077399921 0.35798268 0.66099199 0.96044053 0.077399921 0.35798268 0.66099199 0.96044053 0.096936364 NaN NaN 0.95641705 0.077704355 0.35960730 0.66544664 0.96462831 0.77566164 0.20423820 0.19140617 0.075323097 0.33880119 0.62680637 0.92161635 0.70466609 0.19663292 0.18165617 0.19100898 0.20369039 0.78817137 0.77029269 0.077399921 0.35798268 0.66099199 0.96044053 NaN NaN NaN

(Calculated reflectance for each region. Nan if there is no selection or no lab reflectance model for the region)

camera id, filter number, rad-to-iof scaling factor, uncertainty

4007 1 6.9130400 0.39587878

(camera id, filter number, calculated rad-to-iof scaling factor, uncertainty in the scaling factor)